

The Young and the Wild: What happens to Protoclusters forming at $z \approx 4$?

RHEA-SILVIA REMUS,¹ KLAUS DOLAG,^{1,2} and HELMUT DANNERBAUER^{3,4}

¹*Universitäts-Sternwarte München, Fakultät für Physik, Ludwig-Maximilians-Universität, Scheinerstr. 1, D-81679 München, Germany*

²*Max-Planck-Institute for Astrophysics, Karl-Schwarzschild-Str. 1, D-85748 Garching, Germany*

³*Instituto de Astrofísica de Canarias, E-38205 La Laguna, Tenerife, Spain*

⁴*Universidad de La Laguna Dpto. Astrofísica, E-38206 La Laguna, Tenerife, Spain*

(Received August 3, 2022; Revised August 3, 2022; Accepted August 3, 2022)

Submitted to ApJ

ABSTRACT

Using one of the largest volumes of the hydrodynamical cosmological simulation suit *Magneticum*, we study the evolution of protoclusters identified at redshift ≈ 4 , with properties similar to *SPT2349-56*. We identify 42 protoclusters in the simulation, as massive and equally rich in substructures as observed, confirming that these structures are already virialized. The dynamics of the internally fast rotating member galaxies within these protoclusters resembles observations, merging rapidly to form the cores of the BCGs of the assembling clusters. Half of the gas reservoir of these structures is in a hot phase, with the metal-enrichment at a very early stage. These systems show a good agreement with the observed amount of cold star-forming gas, largely enriched to solar values. We predict that some of the member galaxies are already quenched at $z \approx 4$, rendering them undetectable through measurements of their gas reservoir. Tracing the evolution of protoclusters reveals that none of the typical mass indicators at high redshift are good tracers to predict the present-day mass of the system. We find that none of the simulated protoclusters with properties as *SPT2349-56* at $z = 4.3$, are among the top ten most massive clusters at redshift $z = 0$, with some barely reaching masses of $M \approx 2 \times 10^{14} M_{\odot}$. Although the average star-formation and mass-growth rates in the simulated galaxies match observations at high redshift reasonably well, the simulation fails to reproduce the extremely high total star-formation rates within observed protoclusters, indicating that the sub-grid models are lacking the ability to reproduce higher star-formation efficiency (or lower depletion timescales).

Keywords: galaxies: clusters: general – high-redshift – formation – evolution – methods: numerical

1. INTRODUCTION

Overdensities of galaxies at very high redshifts have been observed in increasingly large amounts in the last few years, reaching redshifts as high as $z = 6$ and more. Assuming that those massive agglomerations of galaxies are the cores of structures that will collapse into very massive galaxy clusters at present day, these structures have been named *protoclusters* (see Overzier 2016, for an overview). Structures that will eventually collapse into a massive galaxy cluster by $z = 0$ are stretched out over several tenth to hundreds of Mpc (Muldrew et al. 2015, e.g.), and the galaxy overdensities that are observed thus are only the (possibly already collapsed) cores of these structures. However, naming has been imprecise here, with the term protocluster being used usually for what are the cores of the assembling structures.

Some of these observed protocluster cores reach masses high enough to challenge predictions from Λ CDM cosmological simulations, for example the two massive protoclusters observed at $z \approx 4$, namely *SPT2349-56* at $z = 4.3$ (Miller et al. 2018; Roter-mund et al. 2021) with a total mass of more than $1 \times 10^{13} M_{\odot}$, and the even more massive protocluster reported by Oteo et al. (2018) at $z = 4.0$ with a total mass above $4 \times 10^{13} M_{\odot}$. Both of these protocluster cores have large numbers of member galaxies with extremely high total star formation rates of more than $6000 M_{\odot}/\text{yr}$. Even more challenging is the structure reported by Chanchaiworawit et al. (2019) at $z = 6.5$ with a virialized core mass of $M_{200} \approx 4.06 \times 10^{13} M_{\odot}$. Many more such overdensities at redshifts of $z = 4$ and higher have been recently reported (e.g., Ouchi et al. 2005; Toshikawa et al. 2012, 2014; Harikane et al. 2019; Calvi et al. 2019; Toshikawa et al. 2020; Calvi et al. 2021), with still large masses but not as extreme.

At lower redshift of about $z \approx 2$, several protocluster cores have been already observed. One of the first reported and by now best studied protoclusters at this

redshift is the so-called Spiderweb-galaxy at $z = 2.16$, which actually consists of several galaxies with extremely high star formation rates (Dannerbauer et al. 2014; Shimakawa et al. 2014, 2018), larger than what is reported for the star forming main sequence at these redshifts (Santini et al. 2017; Pearson et al. 2018), and often they are associated with massive star forming submillimeter galaxies (e.g., Zhang et al. 2022). Extremely high star formation rates for both the whole protocluster core but also the individual galaxies in these cores have been confirmed for other protocluster cores as well from redshifts $4 < z < 2$ (e.g., Umehata et al. 2015; Wang et al. 2016; Kubo et al. 2016, 2017; Wang et al. 2018), especially through observations of CO with ALMA. Strazzullo et al. (2018) especially used CO observations of clusters at $z \approx 2$ to show that the star formation rates in these clusters are strongly enhanced compared to the field. However, while Aoyama et al. (2022) reported for their protocluster at $z \approx 2.5$ rather high star formation rates, they cannot confirm that these are higher than what is seen for star forming galaxies of the same mass in the field.

While many of the galaxies in such protoclusters seem to have enhanced star formation rates, some already quenched galaxies have also been reported. For example, (Kubo et al. 2013) already reported a quiescent fraction of about 20...50% in a protocluster region at $z = 3.1$, while McConachie et al. (2022) confirm even a quiescent fraction of 70% in a protocluster core at $z = 3.37$, and Shi et al. (2019) found an enhancement of quiescent galaxies in a protocluster structure at $z = 3.78$. A clear environmental dependence of the quenched fraction of galaxies can be already found around $3 < z < 2$ (Kodama et al. 2007; Yonekura et al. 2021), and for redshifts between $1 < z < 2$, quenched fractions have been shown to increase with lower redshifts in clusters (e.g., Cooke et al. 2019; Sarron & Conselice 2021) especially compared to the field (Cooke et al. 2019). The red sequence buildup is clearly apparent in galaxy clusters $z = 2$ and below (Strazzullo et al. 2013; Hatch et al. 2017; Strazzullo et al. 2016; Ando et al. 2022), suggesting that agglomeration of red sequence galaxies could be good tracers for (proto)clusters at high redshifts (Strazzullo et al. 2015), albeit detections of such quiescent galaxies are still rare above $z = 3$, see for example Kubo et al. (2021). This is in agreement with simulations that report the morphology density relation to be building up around $z = 2$ (Teklu et al. 2017).

From the simulation side, the evolution of galaxy clusters has been predicted to high redshifts from models and dark matter only cosmological simulations so far (e.g., Chiang et al. 2013; Muldrew et al. 2015), as extremely large fully hydrodynamical cosmological simulations are expensive and thus still rare, but required to reproduce massive collapsed protoclusters at

high redshifts. However, zoom-simulations of individual galaxy clusters have been used to study the star formation properties of protocluster galaxies (Bassini et al. 2020), but also especially the build-up of the cores of today's most massive galaxies, the brightest cluster galaxies (BCGs) (Ragone-Figueroa et al. 2018; Rennehan et al. 2020).

There are various and sometimes not concordantly used denotations of protoclusters and protocluster cores in the literature, with the exact terminology still a matter of debate. As we are using data from simulations in this work, we have the full 3D and evolution information for all our simulated structures, and thus we will stick to a strictly physically motivated definition, calling the virialized¹ regions identified in the simulations at a given redshift *protocluster*, as they are already bound structures with a common dark matter halo. We will call the Lagrangian region, which comprised everything that will end up in the final galaxy cluster at $z = 0$, *protocluster region*, and the central region, which can be associated with the forming BCG, the *protocluster core*. Note that we will *not* attempt to find protocluster candidates by associations of galaxies, as observer would do. We would suggest to call these *protocluster associations*.

In this study, we will use one of the largest fully baryonic cosmological hydrodynamical simulation volumes from the *Magneticum* pathfinder simulation suite, which we will introduce in Sec. 2, to identify for the first time protocluster core counterparts to those observed at $z \approx 4$ and study their properties in Sec. 3, including member star formation rates and quiescent fractions. Using the full power of the simulations, we will track those protocluster cores and their galaxies down to $z = 0$ in Sec. 4, also studying the impact of the cosmological parameters as well as the importance of simulation volumes in finding overdensities as massive as those currently observed, predicting maximum observable virialized masses up to $z = 10$. Finally, in Sec. 5, we will summarize and discuss the results.

2. THE MAGNETICUM PATHFINDER SIMULATIONS

To find protoclusters at high redshift comparable to those observed recently in mass, a large fully baryonic simulation volume is required. For the major part of this study we use one of the largest volumes from the hydrodynamical cosmological simulation suite *Mag-*

¹ Note that in simulations virialized structures are defined via a density contrast predicted from spherical Top-Hat models. The protocluster structures, however, are fast growing, so the virial ratio here should also including the surface term and should not be confused with being a static system. Nevertheless, the velocity dispersion of the member galaxies typically reflects the virial velocity of the halo in good approximation.

*neticum Pathfinder*² (Dolag et al., 2021, in prep), for which the resolution is high enough to resolve galaxies down to baryonic masses of $M_{\text{bar}} > 10^{10} M_{\odot}$. This simulation, *Box 2b* (see Bocquet et al. 2016; Ragagnin et al. 2019, Kimmig et al., in prep.), has a box-size of $(640 \text{ Mpc}/h)^3$ and a particle mass resolution of $m_{\text{DM}} = 6.9 \times 10^8 M_{\odot}/h$ and $m_{\text{Gas}} = 1.4 \times 10^8 M_{\odot}/h$ for dark matter and gas, respectively. Since each gas particle can spawn up to four stellar particles during its lifetime, the mass of a stellar particle is approximately $m_* \simeq 3.5 \times 10^7 M_{\odot}/h$. For dark matter and gas particles the same softening is used, with $\epsilon_{\text{DM}} = \epsilon_{\text{Gas}} = 3.75 \text{ kpc}/h$, while for the stars a softening of $\epsilon_* = 2 \text{ kpc}/h$ was adopted. For more details on this specific simulation and its clusters and galaxies at low redshifts, see Remus et al. (2017); Lotz et al. (2019); Harris et al. (2020); Lotz et al. (2021).

The Magneticum simulations adapt a ΛCDM cosmology (Komatsu et al. 2011), i.e. $\sigma_8 = 0.809$, $h = 0.704$, $\Omega_{\Lambda} = 0.728$, $\Omega_{\text{m}} = 0.272$, and $\Omega_{\text{b}} = 0.0451$. For the initial slope of the power spectrum, a value of $n_s = 0.963$ is used. The simulation was performed with an updated version of GADGET-3, including, in addition to various modifications in the formulation of SPH (Dolag et al. 2004, 2005; Donert et al. 2013; Beck et al. 2016), modernised versions of the sub-grid physics, especially with respect to the star formation and metal enrichment descriptions (Tornatore et al. 2004, 2007; Wiersma et al. 2009), and the black hole feedback (Fabjan et al. 2010; Hirschmann et al. 2014). For more details on the physics included in the Magneticum Pathfinder simulations, we refer the reader to Hirschmann et al. (2014), Teklu et al. (2015), and Dolag et al. (2017).

The data of these simulations up to redshift $z \approx 2$ are publicly available on the *Cosmological Web Portal*³, see Ragagnin et al. (2017). In general, the main suite of the Magneticum simulations encompasses five different simulation volumes: *Box 0* with a box-length of $(2688 \text{ Mpc}/h)^3$, *Box 1* with a box-length of $(896 \text{ Mpc}/h)^3$, *Box 2b* with a box-length of $(640 \text{ Mpc}/h)^3$, *Box 3* with a box-length of $(128 \text{ Mpc}/h)^3$, and *Box 4* with a box-length of $(48 \text{ Mpc}/h)^3$, all adopting the same physics and cosmology as described above. In addition, the Magneticum simulations include a set of 15 simulations of the *Box 1* volume with a resolution of 2×1526^3 particles, adopting different cosmologies with varying σ_8 , H_0 , Ω_0 , and Ω_{b} . These simulations have been introduced by Singh et al. (2019).

For all simulations, structures are identified using a modified version of SUBFIND (Springel et al. 2001; Dolag et al. 2009). Total masses (baryonic and dark matter) are calculated in case of M_{vir} from the Top-

Hat model, with the virial radius R_{vir} the radius of the sphere that would include the virial mass in case the structure would be relaxed and virialized. This is, of course, a very poor assumption especially at high redshifts, and thus the virial radius is not necessarily a good prescription of the actual radial distribution of the structure.

3. PROTOCLUSTERS AT $z \approx 4$

As the recently detected massive protoclusters or protocluster cores are at redshifts of about $z \approx 4$ (Miller et al. 2018; Oteo et al. 2018; Rotermund et al. 2021), we select our protocluster candidates at a similar redshift snapshot of $z = 4.2$. These protoclusters or protocluster cores consist of several galaxies clustered in a very small volume. However, it is not known for sure from observations that such structures are already bound, albeit it is very clear that they are already linked together. Therefore, we select our protocluster candidates based on the total mass that is already linked together by a Friends-of-Friends algorithm with a linking length of 0.2. At $z = 4.2$, this provides us with 42 structures with total masses above $M_{\text{tot}} = 1 \times 10^{13} M_{\odot}$.

However, this is not a possible detection criterion for observations, so we refine our selection criteria from this pool of protocluster candidates based on the following four methods that closely mimic observational methods: First, as the galaxies observed in these protoclusters are in close vicinity and from their velocities they indicate that they are already bound, we assume that these protocluster cores are already bound structures, and thus assume that they are already virialized⁴. This delivers the most massive and concentrated structure at that redshift, and we find the most massive system having a total mass of $M_{\text{vir}} = 2.148 \times 10^{13} M_{\odot}$. Tab. 1 lists the 16 most massive bound structures in our simulation at $z = 4.22$ according to their total (virial) mass (upper part).

A second approach is to identify protoclusters based on an already very massive central galaxy (a proto-BCG), with several smaller galaxies in close vicinity. The lower part of Tab. 1 lists the 16 protocluster candidates with the most massive stellar galaxy M_{CD} . As can be seen immediately from this table, there is no direct correlation between the total mass of the protocluster candidates and the stellar mass of the most massive galaxy in the structure; in fact, only half of the structures with the highest total mass are present in the list of 16 structures with the most massive stellar components. This already indicates that there is no simple indicator that uniquely

² www.magneticum.org

³ https://c2pacosmosim.uc.lrz.de/

⁴ Here we use M_{vir} , the density contrast calculated from the Top-Hat model. These values (and the ranking) will slightly change if we use $M_{200\text{crit}}$ or $M_{200\text{mean}}$.

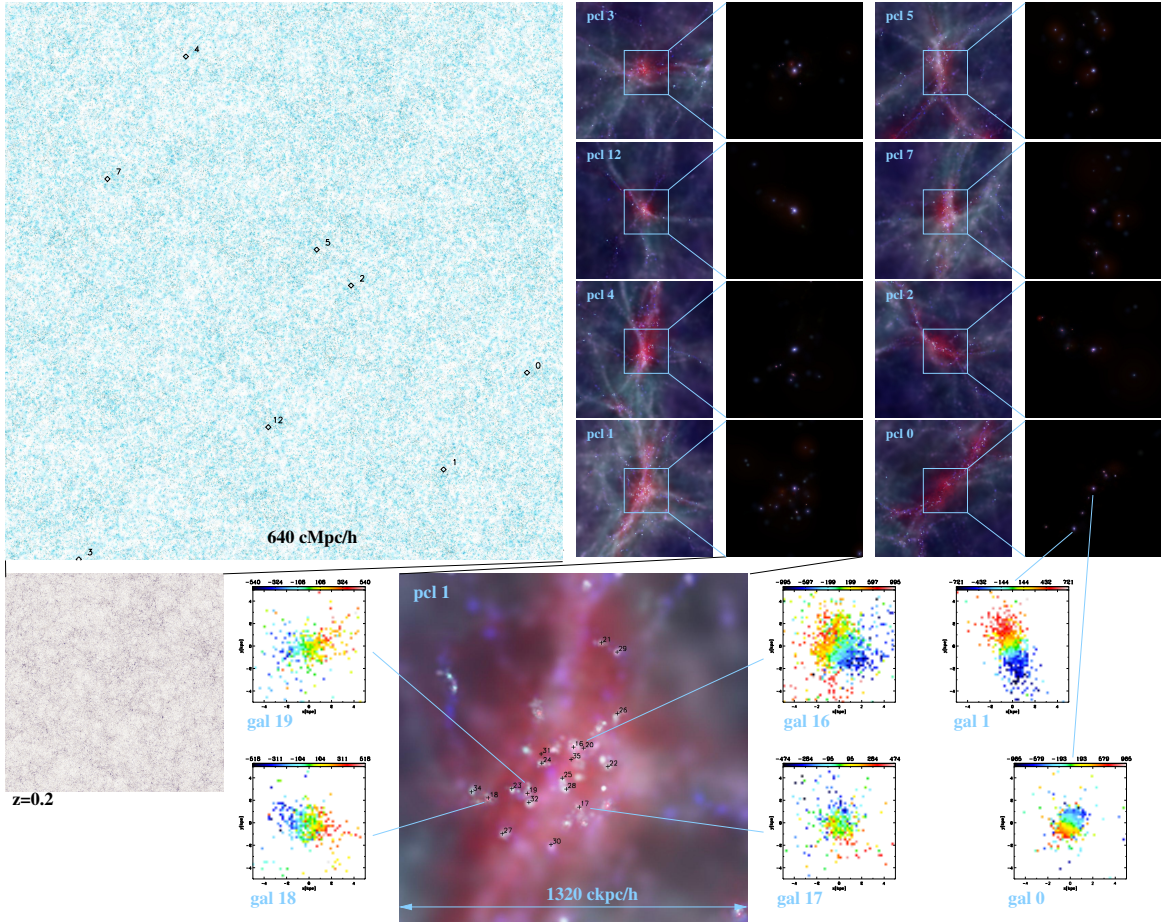


Figure 1. *Upper left:* Stellar distribution of *Magneticum Box 2b* at $z = 4.2$, with the labeled locations of the protoclusters PCl 3/12/0/5/1/7/2/4. *Upper right:* Zoom-in on the 8 selected protoclusters, with the left panels showing the gas content, from cold (blue) to hot (red), and the right panels showing a zoom on the central stellar components within 1320 kpc/h co-moving, which corresponds to a physical box length of 353.77 kpc, with the colors marking the age of the stars (from young (blue) to old (red)). *Lower right:* Larger version of the central area of PCl 1 with both gas and stars shown in the same color scheme as in the small panels, with a box-length of 353.77 kpc. The galaxies are labeled according to their stellar mass. In addition, the rotation maps of the gas are shown for six example galaxies, four from PCl 1 and two from PCl 0. *Lower left:* Stellar distribution of the *Magneticum Box 2b* volume at $z = 0$.

links the total mass growth and the growth of the stellar components at this epoch.

However, observationally the total (or dynamical) mass is difficult to measure, and structures at high redshift are usually detected due to their extreme luminosity indicative of high amounts of star formation, or due to their overdensity in number of galaxies. Therefore, with method 3 we also select 16 protocluster candidates as the most star forming structures at $z = 4.2$ (see upper part of Tab. 2). Interestingly, the structure with the highest star formation rate of $\text{sfr} = 2858.06 M_{\odot}/\text{yr}$ is the second most massive structure in our simulation box, and the three most star forming structures are all among the 16 most massive structures. However, similar to what we found for the stellar mass of the most massive galaxy, about half of the most star forming structures are not among the most massive structures in our sample.

Additionally, we also select the 16 structures with the highest number of galaxies at $z = 4.2$ (see lower part of Tab. 2), with the richest structure hosting

25 galaxies, all of which are star forming. This structure has, in fact, a total mass of only $M_{\text{vir}} = 9.83 \times 10^{12} M_{\odot}$, and thus is definitely not among the 42 most massive structures in our simulation at $z = 4.2$. Here, we find a first very interesting tendency: From the 16 richest structures, only three are among the 16 most massive structures in our simulation box, clearly indicating that richness in member numbers is not a good tracer for the most massive structures at redshifts as high as $z = 4.2$.

3.1. Selecting a set of protoclusters at $z = 4.2$

From each of the four categories introduced above, we now choose a total of 8 protoclusters to study in more detail in this work, which we will call protoclusters (PCl) in the following and which are highlighted in gray in tables 1 and 2: PCl 0, PCl 1, PCl 2, PCl 3, PCl 4, PCl 5, PCl 7, and PCl 12. Images of all these 8 clusters can be seen in the upper right panels of Fig. 1, with each left panel showing the gas of the protocluster and its environment, and the right panel showing

Table 1. Details of the 16 highest-ranked protocluster candidates at $z = 4.2$, selected according to their total (dark plus baryonic) mass M_{vir} calculated from the Top-Hat model (upper table block), and according to the stellar mass of their most massive galaxy M_{CD} (lower table block). The mass rank refers to the total (dark plus baryonic) mass at the given redshift. N_{gal} is the total number of galaxies inside the protocluster, with N_{sf} and N_{qui} referring to the number of star forming and quiescent cluster member galaxies, respectively, with galaxies with $sSFR < 0.3 \times t_{\text{Hub}}$ defined as quiescent. M_* is the total stellar mass inside the virial radius, including all member galaxies as well as the ICM. SFR_{total} refers to the star formation rate inside the whole protocluster, summed over all galaxy members. The last two columns are the virial mass M_{vir} and the mass rank of the protoclusters at $z = 0$. The eight protoclusters that we study in more detail in this work are highlighted in gray if they are part of the respective 16 highest-ranks.

ID	mass rank ($z = 4.2$)	M_{vir} [$10^{13} M_{\odot}$]	M_{CD} [$10^{11} M_{\odot}$]	N_{gal}	M_* [$10^{11} M_{\odot}$]	SFR_{total} [M_{\odot}/yr]	N_{sf}	N_{qui}	$M_{\text{vir}}(z = 0)$ [$10^{14} M_{\odot}$]	mass rank ($z = 0$)
0	0	2.148	3.668	14	11.965	2295.31	14	0	14.332	6
3	1	2.006	4.995	11	9.541	2858.06	10	1	7.608	67
2	2	1.971	5.661	9	9.536	1511.79	8	1	3.049	776
4	3	1.954	8.553	10	9.767	1664.15	10	0	4.229	341
1	4	1.702	5.735	19	9.278	1875.30	17	2	10.156	32
13	5	1.568	4.452	9	6.624	1937.18	9	0	5.269	207
8	6	1.565	3.868	13	8.925	1918.91	12	1	3.185	702
12	7	1.543	5.823	6	7.053	2651.89	6	0	1.334	3666
6	8	1.473	5.713	8	9.908	1751.19	6	2	6.530	106
14	9	1.445	4.640	7	7.695	1377.81	5	2	5.623	165
11	10	1.422	7.353	7	8.717	1959.89	6	1	2.291	1364
18	11	1.394	4.608	15	6.136	1525.29	13	2	10.727	25
26	12	1.381	4.786	9	6.339	1205.19	9	0	0.324	27831
21	13	1.359	6.354	8	7.034	948.03	4	4	13.964	10
15	14	1.358	7.409	7	7.754	1419.14	6	1	2.072	1665
23	15	1.349	3.849	9	5.711	1809.63	8	1	3.832	447
4	3	1.954	8.553	10	9.767	1664.15	10	0	4.229	341
16	17	1.299	8.404	6	8.450	1335.22	3	3	1.476	3073
15	14	1.358	7.409	7	7.754	1419.14	6	1	2.072	1665
11	10	1.422	7.353	7	8.717	1959.89	6	1	2.291	1364
25	18	1.250	7.017	3	7.479	1452.07	3	0	11.603	18
21	13	1.359	6.354	8	7.034	948.03	4	4	13.964	10
63	46	0.950	6.184	2	6.215	1023.38	1	1	1.156	4634
36	31	1.090	5.849	7	5.983	1383.49	6	1	3.973	409
12	7	1.543	5.823	6	7.053	2651.89	6	0	1.334	3666
70	52	0.922	5.763	2	5.769	1148.47	1	1	1.504	2967
1	4	1.702	5.735	19	9.278	1875.30	17	2	10.156	32
6	8	1.473	5.713	8	9.908	1751.19	6	2	6.530	106
2	2	1.971	5.661	9	9.536	1511.79	8	1	3.049	776
69	54	0.916	5.655	2	5.762	919.90	2	0	4.412	313
49	34	1.064	5.603	4	5.884	1408.18	4	0	2.984	802
34	25	1.163	5.598	6	6.200	1181.58	5	1	1.150	4668

the stellar particles in the innermost 1329 kpc/ h co-moving (which is 353.77 kpc physical at $z = 4.2$), centered around the protocluster core. In particular, those 8 clusters were chosen as follows: PCl 3, PCl 12, PCl 0, and PCl 5 are the four protoclusters with the highest star formation rates, PCl 1 also being among the 16 protoclusters with the highest star formation rates (rank 11); PCl 5, PCl 1, and PCl 7 are the three richest protoclusters in terms of galaxy membership, with PCl 0 also being among the 16 richest protoclusters (rank 12); PCl 0, PCl 3, PCl 2, PCl 4, and

PCl 1 are the most massive protoclusters with respect to the total mass, with PCl 12 being also among the 16 most massive ones (rank 7); Finally, PCl 4 is the structure with the most massive stellar galaxy, with the central galaxies of PCl 1 and PCl 2 also belonging to the 16 most massive central galaxies (rank 10 and 12, respectively).

PCl 1 is the only protocluster that is part of all four categories, and its innermost part is shown in the lower central panel of Fig. 1 with both stars and gas, with gas rotation maps shown for four of its most

Table 2. Same as Tab. 1 but for the 16 highest-ranking protocluster candidates at $z = 4.2$ selected according to their total star formation rate $\text{sfr}_{\text{total}}$ (upper table block), and their total number of member galaxies N_{gal} (lower table block).

ID	mass rank ($z = 4.2$)	M_{vir} [$10^{13} M_{\odot}$]	M_{CD} [$10^{11} M_{\odot}$]	N_{gal}	M_{*} [$10^{11} M_{\odot}$]	$\text{SFR}_{\text{total}}$ [M_{\odot}/yr]	N_{sf}	N_{qui}	$M_{\text{vir}}(z = 0)$ $10^{14} [M_{\odot}]$	mass rank ($z = 0$)
3	1	2.006	4.995	11	9.541	2858.06	10	1	7.608	67
12	7	1.543	5.823	6	7.053	2651.89	6	0	1.334	3666
0	0	2.148	3.668	14	11.965	2295.31	14	0	14.332	6
5	43	0.983	2.261	25	7.341	2115.63	25	0	10.742	24
141	88	0.799	3.902	6	4.170	2061.60	5	1	4.421	311
157	124	0.743	3.787	6	3.947	1999.84	5	1	0.765	8708
10	30	1.113	2.746	14	7.568	1985.91	13	1	8.756	44
11	10	1.422	7.353	7	8.717	1959.89	6	1	2.291	1364
13	5	1.568	4.452	9	6.624	1937.18	9	0	5.269	207
8	6	1.565	3.868	13	8.925	1918.91	12	1	3.185	702
64	37	1.030	4.177	4	4.581	1916.37	3	1	1.464	3124
1	4	1.702	5.735	19	9.278	1875.30	17	2	10.156	32
85	183	0.677	2.130	7	4.282	1811.17	6	1	0.819	7864
23	15	1.349	3.849	9	5.711	1809.63	8	1	3.832	447
24	21	1.225	3.337	10	5.476	1789.22	9	1	11.655	17
6	8	1.473	5.713	8	9.908	1751.19	6	2	6.530	106
5	43	0.983	2.261	25	7.341	2115.63	25	0	10.742	24
1	4	1.702	5.735	19	9.278	1875.30	17	2	10.156	32
7	92	0.792	4.498	18	8.507	1484.96	16	2	10.344	29
54	304	0.598	2.378	16	4.512	1349.63	16	0	6.042	130
42	82	0.821	1.588	16	4.301	1264.03	14	2	15.947	3
45	59	0.897	1.561	16	4.760	1095.77	15	1	16.091	2
32	51	0.923	0.888	16	5.162	1294.38	15	1	3.388	610
19	36	1.030	4.999	15	6.304	1525.21	15	0	3.631	519
20	29	1.120	2.322	15	5.413	1390.69	13	2	6.279	115
18	11	1.394	4.607	15	6.136	1525.29	13	2	10.727	25
56	286	0.607	1.534	14	4.393	990.11	14	0	0.791	8280
10	30	1.113	2.746	14	7.568	1985.91	13	1	8.756	44
0	0	2.148	3.668	14	11.965	2295.31	14	0	14.332	6
110	466	0.529	0.561	13	3.892	1023.11	13	0	2.940	821
30	172	0.686	2.465	13	5.481	1192.98	13	0	3.657	508
66	110	0.760	1.806	13	4.215	1175.05	12	1	1.659	2516

gas-rich galaxy members. Interestingly, the properties of our PCl 1 are strikingly similar to those found for *SPT2349-56* (Miller et al. 2018; Rotermund et al. 2021): PCl 1 has a BCG stellar mass of $M_{\text{CD}} = 5.7 \times 10^{11} M_{\odot}$, while the BCG found for *SPT2349-56* has been reported to have $M_{\text{BCG}} = 3.2 \times 10^{11} M_{\odot}$; PCl 1 has 19 member galaxies above $M_{\text{bar}} > 10^{10} M_{\odot}$, while there are so far 14 member galaxies reported for *SPT2349-56*. And the total stellar mass reported for the central part of *SPT2349-56* is about $M_{*} = 1.2 \times 10^{12} M_{\odot}$, while the total stellar mass in the virialized region of PCl 1 is $M_{*} = 9.3 \times 10^{11} M_{\odot}$. Gas rotation maps are also shown for two gas-rich galaxies from PCl 0, which is part of three of our four protocluster candidate selection criteria.

The cold gas disks in those gas-rich galaxies found in our protoclusters are of similar gas masses as those

observed at high redshifts (e.g., Dannerbauer et al. 2017), and are typically all rotating at rather high velocities of about 200-600 km/s, which is slightly higher than the values reported from observations so far (Smit et al. 2018; Jones et al. 2021), albeit these observed galaxies are not inside protoclusters but rather identified due to their high UV luminosity, and thus they are not directly comparable to the galaxies inside protoclusters shown in this work. As can be seen from the upper left panel of Fig. 1, all of the protoclusters sit at knots of the cosmic filaments, having already a heated atmosphere and accrete galaxies and mostly cold gas along the filaments, which penetrate deeply into the hot atmosphere. A detailed analysis of the hot atmosphere of these structures is outside the scope of this paper, where we will mainly focus on the properties of the galaxies and the growth of

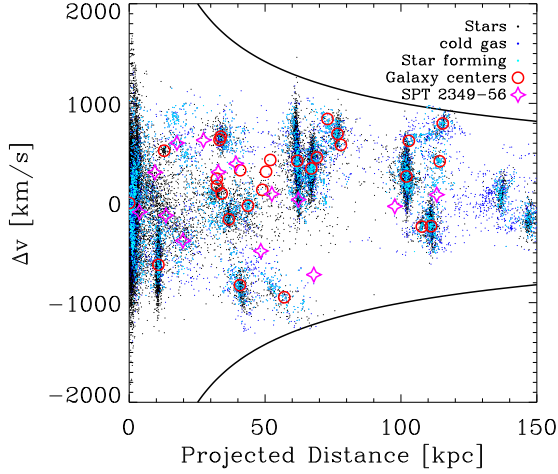


Figure 2. Comparison of the phase-space distribution of the galaxies within *SPT2349-56* (pink open stars) and within our protocluster PCL 1 (red open circles for the centres of mass of the member galaxies). In addition, black small dots mark the stars, blue small dots mark the cold gas particles, and cyan small dots are star-forming gas particles in the individual member galaxies. Black lines mark the escape velocity assuming a relaxed NFW halo for our protocluster PCL 1.

the structures, however, we will quickly discuss some aspects of this in Sec. 3.6. Still, as can be seen in the individual panels of Fig. 1, the geometry of these clusters can be quite different, for example PCL 0 shows a quite striking linear geometry of the main member galaxies, while PCL 12 has a more spherical geometry.

3.2. Properties of the galaxies within protoclusters at $z = 4.2$

The eight protoclusters selected from the simulation can clearly be classified as already bound systems. Note that by construction our selected protoclusters always have to be bound systems, and we can assume that the halo finding based on *SubFind* identifies all such systems in the simulations. Here, we do not intend to find systems which due to projection effects or observational uncertainties could be accidentally identified as spatially close and bound systems although they are not. However, as was shown already in Fig. 1, some of our selected systems have rather linear geometry of the main member galaxies, like PCL 0 but also PCL 1, clearly indicating active ongoing assembly, similar to what is observed for the surroundings of the massive protocluster structures. Thus, comparing the phase-space distributions of the member galaxies from our simulated protoclusters to observations still provides important information about the comparability. Figure 2 shows the phase space distribution of the member galaxies for the protocluster PCL 1 as an example. As can clearly be seen, the velocities of the individual galaxies, although many of them on first in-fall, are all smaller than the escape velocity. In-

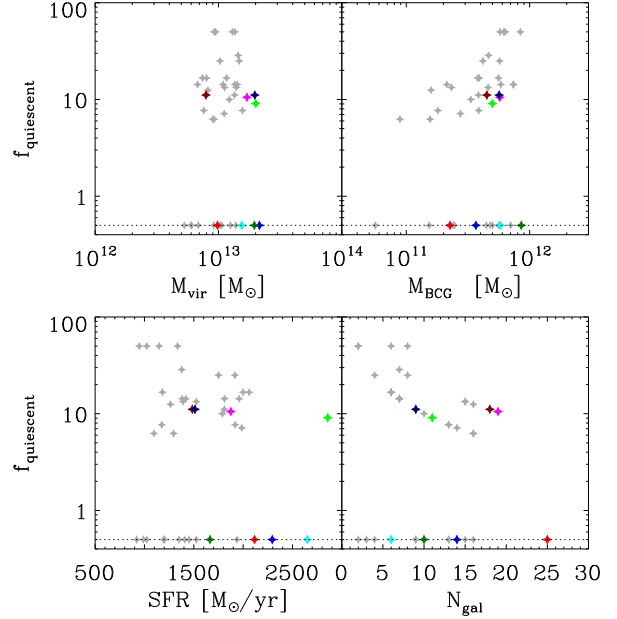


Figure 3. Quiescent fraction for the 42 protocluster candidates versus the four different tracers at $z = 4.2$ used to identify protoclusters: *Upper left:* Quiescent fraction versus virial mass. *Upper right:* Quiescent fraction versus stellar mass of the most massive member galaxy (BCG). *Lower left:* Quiescent fraction versus total star formation rate in the virializes region. *Lower right:* Quiescent fraction versus richness (number of member galaxies in the virialized region). The colored symbols mark the eight specific protoclusters as described in the text, with colors green/cyan/blue/red/magenta/burgundy/darkblue/darkgreen marking PCL 3/12/0/5/1/7/2/4, respectively.

terestingly, the distribution of the individual member galaxies within the phase-space in the simulated protocluster is actually very similar to the distribution reported for *SPT2349-56* (Miller et al. 2018), again highlighting that PCL 1 is in fact a good match for *SPT2349-56*.

3.3. Star formation and quiescent fractions in protoclusters at $z = 4.2$

For all our protoclusters we can also distinguish the star forming from the quiescent galaxies. Following Franx et al. (2008), we use the specific star formation rate $sSFR$, i.e., galaxies with $sSFR < 0.3 \times t_{\text{Hub}}$ are called quiescent, while galaxies with $sSFR > 0.3 \times t_{\text{Hub}}$ are classified as star forming.

3.3.1. Quiescent Fractions

As can be seen from Tab. 1 and Tab. 2, about half of our eight example protoclusters (gray shaded) have no quiescent galaxies yet, while the other half host already one or two quiescent galaxies. Interestingly, the appearance of already quenched galaxies is not related to the virial mass of the system or the amount of member galaxies or the star formation rate. This gets more clear when looking at all 42 protoclusters,

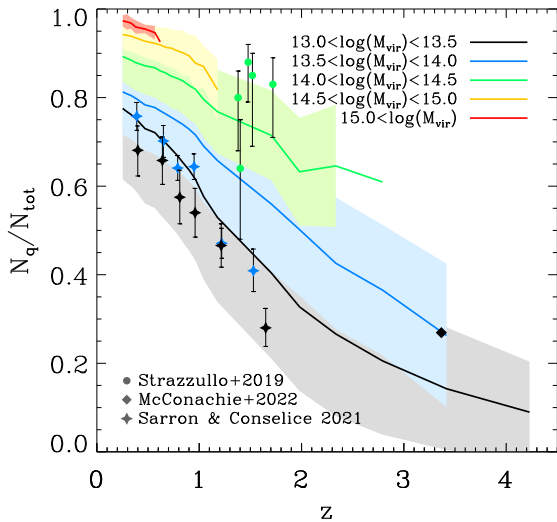


Figure 4. Average fraction of quiescent galaxies with redshift for Magneticum halos of different virial mass ranges, as indicated in the legend. Observations of individual clusters from Strazzullo et al. (2019) are included as circles, and the protocluster from McConachie et al. (2022) is shown as diamond, with the color indicating the mass range of the observed halos compared to the simulated mass range. In addition, stacked mean quiescent fractions from the *Detectivz* survey from Sarron & Conselice (2021) are included as stars, split into two mass bins corresponding to the two lowest simulated mass ranges shown here (Sarron et al., in prep.).

as shown in Fig. 3. Here, also no trend or correlation with the ranking of the protocluster according to the different selection criteria and the appearance of quiescent galaxies can be seen. For example, PCl 5, the protocluster with the highest number of galaxies, has no quiescent galaxy at all, while the protocluster with the largest number of quiescent galaxies, PCl 21, has only 8 galaxies of which half are already quenched. This clearly shows that the quenched fraction at redshifts as high as $z = 4.2$ is not depending on cluster mass, and that environmental quenching at this redshift is not a major quenching mechanism yet, in agreement with previous results that the morphology-density relation only starts to appear around $z = 2$ (e.g., Teklu et al. 2017).

As already demonstrated in earlier work (Lotz et al. 2019), our simulations generally reproduce the observed fraction of quenched galaxies well at $z = 0$ (Lotz et al. 2019) and at $z = 2.7$ (Lustig et al. 2022). Fig. 4 shows the evolution of the quenched fraction depending on host halo mass for five different host halo mass ranges, from $z = 4.2$ to $z = 0$. As expected, the averaged quenched fraction within galaxy clusters (and groups) not only decreases with increasing redshift, but also decreases with halo mass at a fixed redshift. For galaxy clusters above $M_{\text{vir}} = 1 \times 10^{14} M_{\odot}$, the amount of quenched galaxies agrees well with observed quenched fractions from SPT by Strazzullo

et al. (2019) at redshifts up to $z = 1.72$, albeit our average quenched fraction is generally slightly lower than the observed values.

For the lower mass end, we compare our results to observations from the *Detectivz* survey by Sarron & Conselice (2021). This extensive set of observations covers a redshift range up to $z \approx 2$, and the galaxy detection limit in stellar mass is at $M_* \approx 2 \times 10^{10} M_{\odot}$, in good agreement with what we can resolve in our simulations, which enables a comparison with respect to the relative quenched fractions. However, virial masses are not measured directly and need to be modelled, which is why the split into halo masses was done based on the stellar masses and not the halo masses, with the groups sorted into the halo mass bin of $5 \times 10^{13} M_{\odot} < M_{\text{vir}} < 1 \times 10^{14} M_{\odot}$ being selected as having stellar masses of $M_* > 5 \times 10^{11} M_{\odot}$, and those that were sorted into the halo mass bin of $1 \times 10^{13} M_{\odot} < M_{\text{vir}} < 5 \times 10^{13} M_{\odot}$ being selected as having stellar masses of $1 \times 10^{11} M_{\odot} < M_* < 5 \times 10^{11} M_{\odot}$ (private communication, Sarron et al., in prep.). As can be seen from the stars in Fig. 4, the predicted quiescent fractions from the simulations are generally larger than what is observed for the group regime, albeit the lower mass bin agrees reasonably within the errorbars. Whether this is due to the split been made based on halo versus stellar mass, or due to other reasons is beyond the scope of this study.

At redshifts higher than $z = 2$, quiescent fractions are observationally extremely difficult to obtain. Here, we could only include one data point for the protocluster *MAGAZ3NE-J0959* from McConachie et al. (2022) at $z \approx 3.37$, where the total halo mass is also only a rough estimate. Even though this protocluster has most likely a larger than average fraction of quiescent galaxies, it falls well within the upper $1\text{-}\sigma$ range of our predicted quiescent fractions for halos of a total mass of $1 \times 10^{13} M_{\odot} < M_{\text{vir}} < 5 \times 10^{13} M_{\odot}$, indicating that our quenching mechanisms produces reasonable quenched fractions at high redshifts, albeit it is only a single object to compare so far. Adding further observations to this will enhance our understanding of the relevant quenching mechanisms at high redshifts in the future.

3.3.2. Star Forming Galaxies in Protoproclusters

One common finding regarding protoclusters is that models and simulations generally struggle to reproduce the large observed star-formation rates (e.g., Saro et al. 2009) at $z = 2$, Granato et al. (2015) up to $z = 3$, and Lim et al. (2021) up to $z=7$). In the left panel of Fig. 5 we compare the observed integrated star formation rate as function of area on sky of *SPT2349-56* from Miller et al. (2018) with our sample of 8 selected protoclusters. While the BCGs of several of our protoclusters have a star-formation rate which even exceeds the one of the most star-forming galaxy inside the observed protocluster, the sum of all the observed star-formation rates within the same

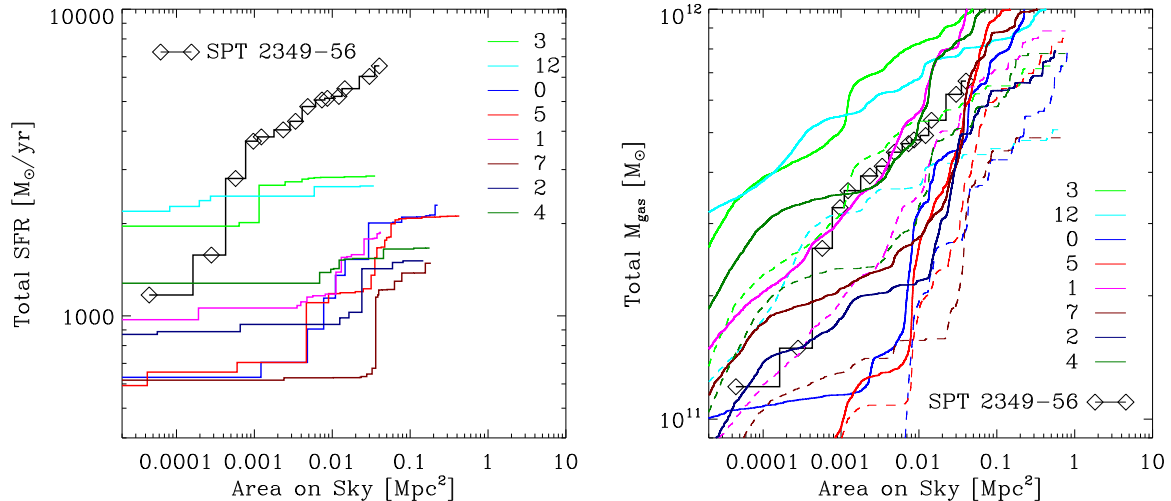


Figure 5. Total star formation rate (left panel) and total gas mass (right panel) versus area-on-sky around the most massive member galaxy for the eight example protoclusters PCI 3/12/0/5/1/7/2/4. The solid lines (colors according to the legend) show the data taken directly from the simulation, while the dashed lines in the right panel show the total gas mass calculated from the gas inside the galaxies alone. For comparison, the values for the protocluster *SPT2349-56* at $z = 4$ from [Miller et al. \(2018\)](#) are shown as black diamonds and solid line.

(virial) area is still a factor of ≈ 3 larger than the one we find in the simulation for all our protoclusters, in agreement with the results found by [Bassini et al. \(2020\)](#) for zoom-in simulations of galaxy clusters.

On the other hand, comparing the amount of available gas between the observations and the simulations, as shown in the right panel of Fig. 5, clearly shows that our protocluster candidates have very similar integrated cold gas mass values as the observations, and several of our protoclusters even exceed the observed gas mass values at all distances from the center. Even if we calculate the available gas only from what is inside the galaxy members of the protoclusters which (mostly) excludes the hot gas component, as shown as dashed lines in the right panel of Fig. 5, some of the protoclusters still reproduce the observed values. Interestingly, the cluster closest in behavior to *SPT2349-56* is again PCI 1, with a nearly identical growth of cold gas mass with distance.

In general, this discrepancy between the observed and simulated star formation rates even though the observed and simulated cold gas reservoirs are in agreement and that is also reported for other simulations (e.g., [Bassini et al. 2020](#)) could have two reasons: Either the simulations in general do not form stars efficiently enough to reproduce the observed values, or the stars are building up at this early times in a much more bursty way compared to the rather continuous rate at which stars are currently formed in simulations.

3.4. Stellar mass function at high redshift

One clear test to answer the questions whether the simulations do generally not form stars efficiently enough is to check how the integrated star-formation

within the simulation compares to observations, i.e., to compare the stellar mass functions at different redshifts. For the Magneticum simulations, it has been shown by [Hirschmann et al. \(2014\)](#) and [Steinborn et al. \(2015\)](#) that the stellar mass function is generally well captured between $z = 4$ and $z = 0$, slightly overshooting the high mass end at $z = 0$. Fig. 6 shows the stellar mass functions for *Box 2b* from $z = 3.4$ to $z = 5.0$. Given that (for data storing reasons) the spacing between available outputs of the simulations is relatively large, comparisons with observations, which typically span certain ranges in redshifts, are more difficult. Therefore, in the left panel of the figure we show the observations binned in the interval $z = 3 \dots 4$ as data points, compared to the simulation at $z = 3.4$. On one hand there is a good agreement at the high mass end, which is the important part for the protoclusters. On the other hand, however, the lack of handling AGN feedback in galaxies below a stellar mass of about $10^{10} M_{\odot}$ due to our resolution limit for the treatment of black holes clearly imprints in an overshooting of the stellar mass function at the low mass end, as a result of slight overcooling at the low mass end. The right panel compares the observations binned in the interval $z = 4 \dots 5$ with the simulation at $z = 4.2$ (blue line) and $z = 5.0$ (red line). Here, the judgment of the agreement between simulations and observations is more difficult, however, given the involved uncertainties in this comparison, the simulations seem to reasonably re-produce the observed stellar mass functions. In summary, we conclude that the description of the averaged star-formation within the simulation seems to reasonably well match the real average star formation within the Universe. Especially, the difference between the observed and sim-

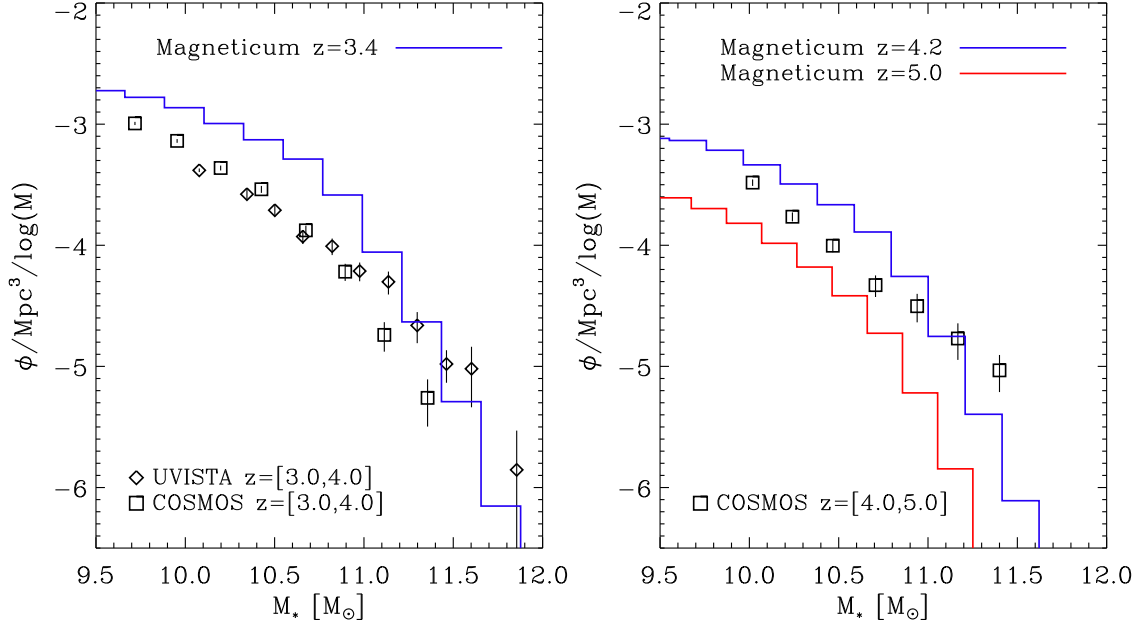


Figure 6. Stellar mass function from the simulation compared to observations from UltraVISTA (Ilbert et al. 2013) and COSMOS (Davidzon et al. 2017). *Left panel:* redshift 3–4; *Right panel:* redshift 4–5.

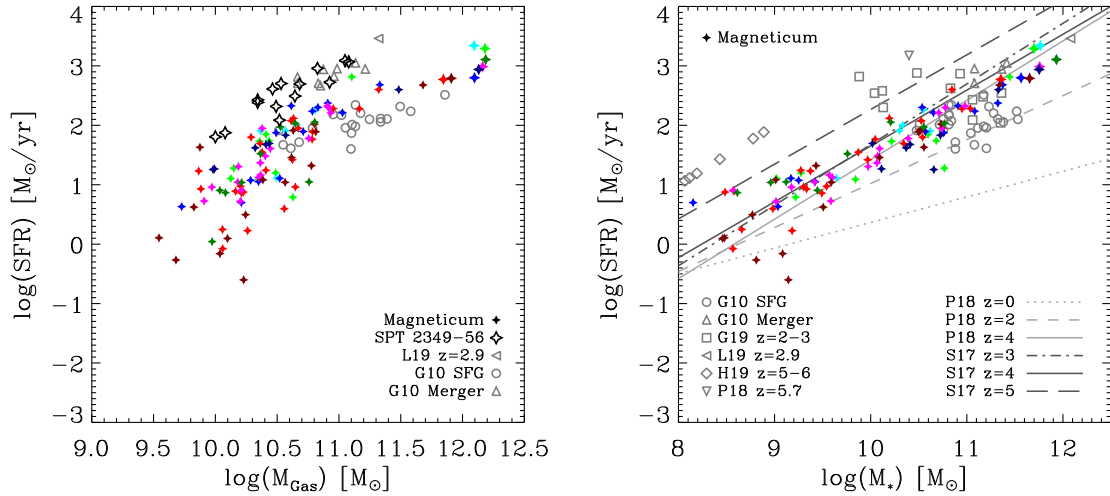


Figure 7. SFR versus M_{Gas} (left panel) and M_* (right panel). Colored stars show the values for the *Magneticum* protocluster galaxies for PC1 3/12/0/5/1/7/2/4 at $z = 4.2$ (colors as in Fig. 5). For comparison, observational values are included as open symbols: In the left panel, the data for the member galaxies from protocluster *SPT 2349-56* at $z = 4$ from Miller et al. (2018) are shown as open black stars, while the gray left-pointing triangle marks the data for the extremely star forming galaxy HXMM05 at $z = 2.9$ from Leung et al. (2019). In addition, the normal star forming (gray circles) and merging (gray upward-pointing triangles) galaxies from Genzel et al. (2010) are shown, which are at redshifts between $z = 1$ and $z = 2$. In the right panel, the same data points as in the left panel for all but the *SPT 2349-56* galaxies are shown with the same symbols. In addition, the value for the starbursting galaxy CRLE at $z = 5.6$ from Pavesi et al. (2018) is shown as downward-pointing gray triangle, values from protocluster members from HELAISS02 ($z = 2.2$), HXMM20 ($z = 2.6$) and CL J1001+0220 ($z = 2.5$) from Gómez-Guijarro et al. (2019) are shown as gray squares, and member galaxies from the most distant spectroscopically confirmed overdensities z57OD ($z = 5.7$) and z66OD ($z = 6.6$) are shown as gray diamonds. Light gray lines show the power-law fits to the star formation main sequence at different redshifts from Herschel (Pearson et al. 2018), while dark gray lines show the corresponding fits from Hubble Frontier Fields measurements (Santini et al. 2017).

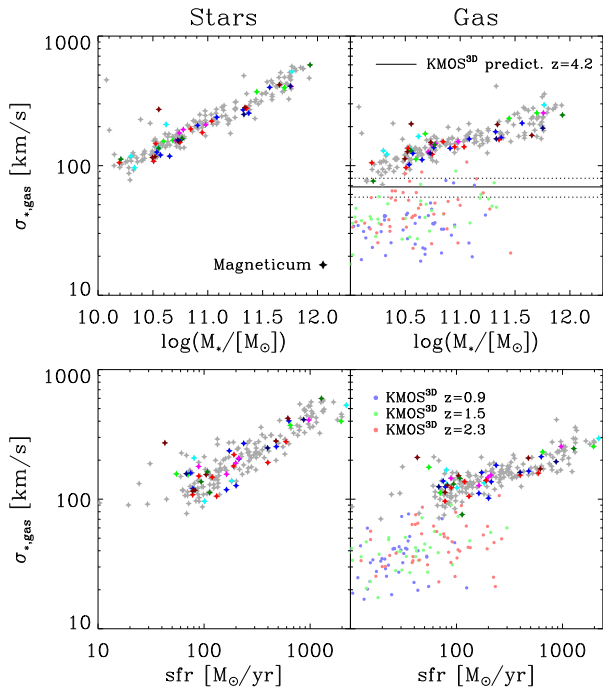


Figure 8. Velocity dispersion within the halfmass radius against stellar mass M_* (*upper panels*) and star formation rate SFR (*lower panels*) for the galaxies in the eight protoclusters colors coded as in Fig. 5, and all protocluster candidates from Tab. 1 and Tab. 2 in gray. *Left panels:* for the stellar component of the galaxies. *Right panels:* for the cold gas component of the galaxies. Observational data from KMOS^{3D} (Übler et al. 2019) are included in the two right panels as colored dots, redshifts as indicated in the label, together with a prediction of the expected value of the velocity dispersion at $z = 4.2$, as extrapolated from their Eq. 1.

ulated stellar mass functions are far smaller than the observed differences in the star formation rates. This again supports our speculation that the difference between the simulations and the observations with respect to the star formation rates at high redshifts is caused by the fact that the simulations do not capture processes which lead to a locally, environment dependent higher star formation efficiency, and therefore the simulations are lacking the extreme star bursting systems, while overall producing the right amount of stars.

3.5. Star formation versus gas reservoir

The overall star formation of galaxies in the Magneticum simulations follows the observed main sequence of star forming galaxies, both when expressed in terms of stellar mass and in form of gas mass over a large range in redshift, as shown in the right panel of Fig. 7. Therefore, the star-formation rate within the galaxies overall are consistent with observations even at the redshift of the protoclusters. However, the simulation misses to reproduce the population of extremely star-forming galaxies as observed in the pro-

toclusters as well as the star-bursting systems (often classified as mergers) at $z = 2$ (e.g. Genzel et al. 2010).

On the other hand, as can be seen in the left panel of Fig. 7, the star formation rates at a given gas mass are much lower than the observed ones, clearly quantifying the issue already seen from Fig. 5, that the gas masses agree well with observations while the star formation rates at the same time are too low. This again indicates that it is not the general, averaged star-formation description which is insufficient in the simulations but rather the simulations are not producing the short depletion times (or large star formation efficiencies) for systems in special conditions or environments. This results in the general stellar and gas masses fitting well with observations, but the individual star formation rates being too low.

Another quantity intricately connected to the stellar and gas masses as well as the star formation rate is the velocity dispersion in the gas disks where the star formation takes place. If the gas disks at high redshift are too turbulent compared to observations, with too large velocity dispersions, this could be another reason for the star formation rates to underperform. As can be seen from the upper panels of Fig. 8, there are tight correlations in the simulations for the stellar masses and the velocity dispersions found for the stellar (left panel) and the cold gas (right panel) components, respectively, as well as between the velocity dispersions and the star formation rate, albeit the correlations between the masses and velocity dispersions is tighter than that found for the velocity dispersions of the components and the star formation rate.

While there are no observations of these correlations at redshifts as high as $z = 4.2$, velocity dispersions of the cold gas have been observed at redshifts up to $z = 2.3$, with predictions for high redshifts from the trends found up to these redshifts (Übler et al. 2019). We included these observations in the right panels of Fig. 8 for comparisons of the general trends found for the correlation between the cold gas velocity dispersions and the stellar mass of the galaxies (upper panel) and the star formation rates (lower panel). Both simulations and observations show a correlation between all three quantities with a similar slope, and a general tendency for the gas velocity dispersions to be higher at higher redshifts. Thus, as far as this comparison is possible, we find general agreement in the trends seen from observations and simulations, however, the absolute velocity dispersions seem to be generally higher than the expected values from the extrapolations of the observations, as indicated by the solid black line in the upper right panel of Fig. 8. This enhanced velocity dispersions are generally seen for simulations even down to redshifts of $z = 0$, see van de Sande et al. (2019), and is most likely a result of the differences in particle mass between dark and baryonic masses and the different softenings used

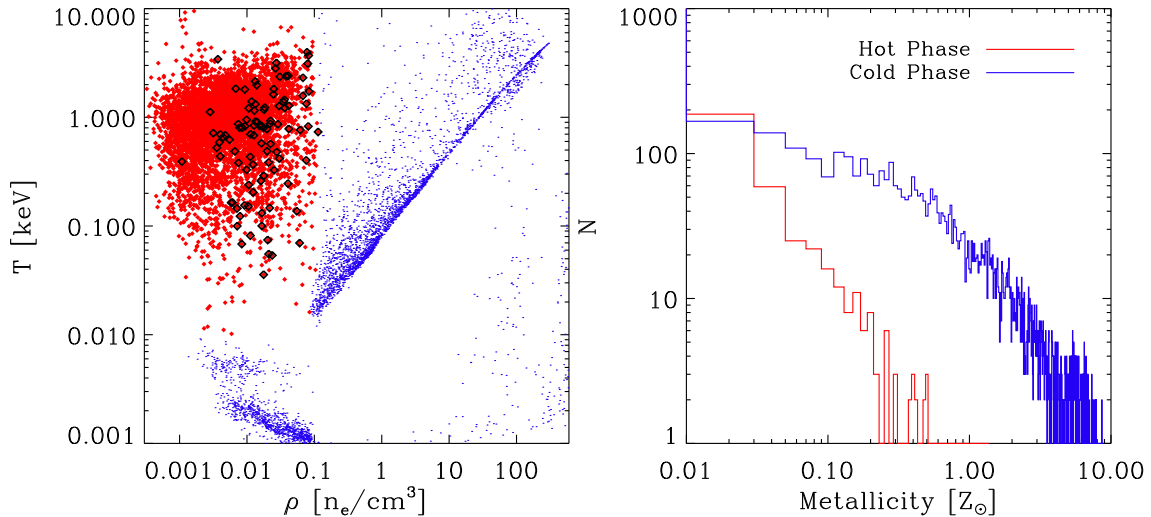


Figure 9. Properties of the gas inside the virial radius of protocluster PCl 1 at $z = 4.2$. *Left panel:* Phase diagram where blue dots are the cold, mostly star-forming gas particles, and red points are the hot ICM phase. Black diamonds mark the small subset of the hot ICM which is already chemically enriched above 10% of the solar value. *Right panel:* Histogram of the chemical enrichment of the cold (blue) and hot (red) phase of the gas.

for different particle types used in the currently available cosmological simulations (Ludlow et al. 2020), and most prominent for disk galaxies (Ludlow et al. 2021). How this affects the star formation properties of galaxies in protocluster environments needs to be studied in the future in more detail.

3.6. Intra Cluster Medium Properties at $z=4.2$

So far, we have discussed the properties of the cold gas component of the galaxies found in the protoclusters, however, the build-up of the hot gaseous halo found in galaxy clusters at present day is already taking place in protoclusters at high redshifts. As an example of the expected state of the gas within protoclusters at $z = 4.2$, the left panel of Fig. 9 shows a phase diagram of the gas within the virial radius of protocluster PCl 1. At this point, roughly half of the baryonic material within the protocluster is still in the cold phase, which is partially star forming. The other half is already in a hot atmosphere, virialized with temperatures centered around $\approx 1\text{keV}$. The presence of gas with temperature of several keV clearly indicates the presence of merger shocks due to the fast growing structures. While the cold and star-forming gas is already largely enriched around solar values, the hot intra cluster medium (ICM) is still mainly metal poor, and only $\approx 2\%$ is already enriched above 10% of the solar abundance. Those metal enriched hot gas is generally in denser parts of the hot halo, as marked by the black diamonds in the left panel of Fig. 9. Based on very similar simulations, Biffi et al. (2017, 2018) demonstrated that some gas which is in the ICM of the present-day clusters was already enriched to solar metallicity at high redshift. This indicates that – as expected – some of the cold, very metal enriched gas

within the protoclusters will be heated by subsequent feedback and stays within the ICM till present-time. Furthermore, this indicates that it could generally be possible to already detect these protoclusters at $z \approx 4$ in X-ray measurements.

4. GALAXY CLUSTER EVOLUTION FROM PROTOCLUSTERS TO PRESENT DAY

Spectacular protocluster cores like *SPT2349-56* are often speculated to be the progenitors of today’s most massive galaxy clusters. In the following we will use the power of the simulations and trace the previously identified protoclusters to $z = 0$.

4.1. Cluster Mass Evolution

While protoclusters surely present very large overdensities at high redshift, the complicated merging process which is involved in the formation of the most massive structures in the Universe leads to a large uncertainty for matching the most massive structures appearing at high redshift to the most massive structures observed at present time. To illustrate this point, Fig. 10 shows the growth of structures in the simulations in comparison with observations at various redshifts. The dark gray band marks the range of virial masses of the 10 most massive systems in the simulations at the different times and very nicely encompasses the observations at various redshifts, indicated by filled symbols in that figure.

The coloured lines show the individual evolution pathways of the 8 example protoclusters. Interestingly, none of them is among the 10 most massive systems at redshift $z = 0$. Some of them even barely reach masses in the galaxy cluster range, and end up

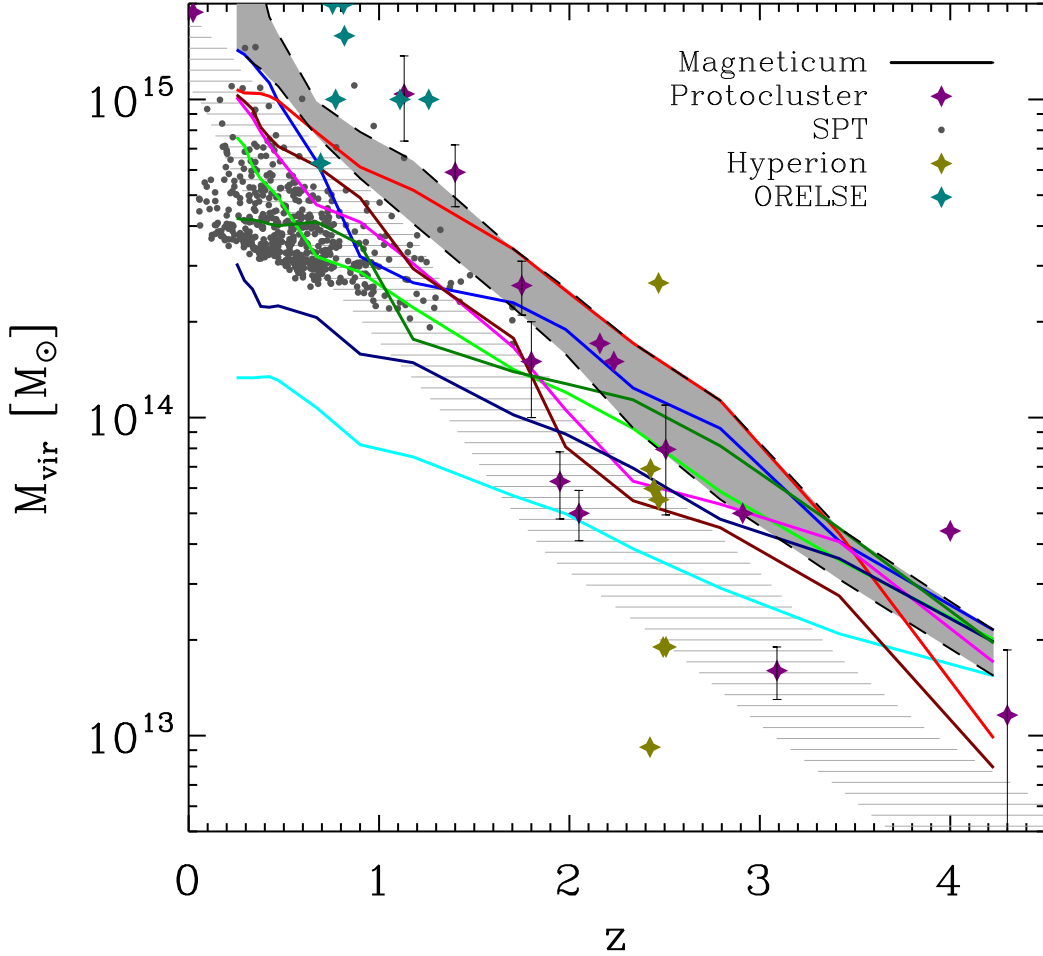


Figure 10. Total cluster mass versus redshift. The colored lines show the evolution of the protoclusters selected at $z = 4.2$, with colors green/cyan/blue/red/magenta/burgundy/darkblue/darkgreen marking the eight different example-protoclusters PCI 3/12/0/5/1/7/2/4, respectively. The grey shaded area marks the mass range of the 15 most massive galaxy clusters in Magneticum *Box 2b* at each redshift, clearly showing that none of the protoclusters selected at $z = 4.2$ is amongst the most massive ones at $z = 0$. Grey filled circles show the SPT clusters taken from Miller et al. (2018), while the lilac stars show individual protoclusters selected with X-ray or optical methods taken from Miller et al. (2018) with additional points for *SPT-CLJ2106-5844* at $z = 1.132$ from Kim et al. (2019), the spiderweb protocluster core at $z = 2.16$ from Shimakawa et al. (2014), SSA22 at $z = 3.09$ from Kubo et al. (2016), the Distant Red Core protocluster at $z = 4.002$ from Oteo et al. (2018), and RO-1001 at $z = 2.91$ from Daddi et al. (2021). Furthermore, the masses and redshifts of the structures from ORELSE by Tomczak et al. (2017) are shown as dark green symbols, and the values for the HYPERION group of merging protoclusters at $z \approx 2.45$ from Cucciati et al. (2018) are shown as light green symbols. In addition, the striped area shows the prediction from Chiang et al. (2013) from the Millenium simulation in combination with a SAM model.

as very low mass cluster systems, like PCI 12 with a final mass of less than $2 \times 10^{14} M_{\odot}$. Some of the most massive clusters at $z = 0$ from our sample of 8 clusters are actually below a mass of $1 \times 10^{13} M_{\odot}$ at $z = 4.2$, and thus below the threshold of what would be considered a protocluster (PCI 1 and PCI 7). From those protoclusters at $z = 4.2$ that are the most massive, only PCI 0 ends up as one of the most massive clusters, although our *SPT2349-56* counterpart PCI 1 also reaches a final mass larger than $1 \times 10^{15} M_{\odot}$.

The weakness of the connection between the ranking of high-mass systems at high redshift with the ranking of the final system mass can also be clearly seen from Tab. 2 and Tab. 1 and the upper left panel

of Fig. 11. Furthermore, Fig. 11 also shows that there is no correlation between the final mass of a cluster at $z = 0$ and either the stellar mass of the most massive galaxy of the total star formation rate of the proto-cluster members. The only quantity for which we find a slight tendency to indicate the outcome of the mass evolution of a protocluster is the richness of the protocluster (see lower right panel of Fig. 11), namely the number of galaxies that are part of the protocluster at $z = 4.2$. This is further supported by what can be seen from Tab. 1 and Tab. 2, namely that the only selection criterion that includes some of the most massive galaxy clusters at present day (mass rank 2 and 3 at $z = 0$), is the selections by richness criterion.

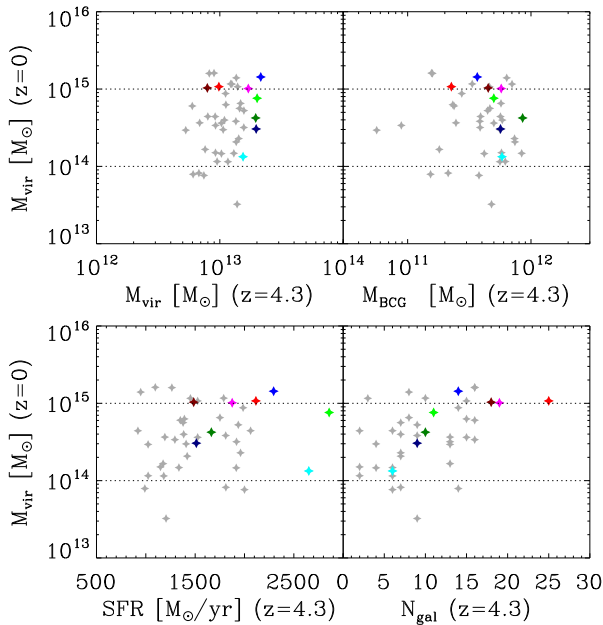


Figure 11. Virial mass at $z = 0$ for the descendants of all protoclusters listed in Tab. 2 and Tab. 1 against the virial mass at $z = 4.2$ (*upper left*), the BCG stellar mass at $z = 4.2$ (*upper right*), the total star formation rate at $z = 4.2$ (*lower left*), and the richness at $z = 4.2$ (*lower right*). The 8 example protoclusters are marked in color, with colors green/cyan/blue/red/magenta/burgundy/darkblue/darkgreen marking PCl 3/12/0/5/1/7/2/4, respectively.

An illustration of why richness is a good tracer while other quantities are not is given in Fig 12. It shows a thin (5 cMpc/h) slice of the large scale structure around the protocluster PCl 1, for which the virial radius at $z = 4.2$ is marked by the yellow circle. All particles of the Lagrangian volume which ends within the virial radius (large gray circle) of the descendant of PCl 1 at present day are shown in color, while the particles that do not end within the cluster are shown in gray. This demonstrates that the protocluster at high redshifts are only the tip of the large scale structures which defines the cluster at present day. Dark red points are tracing gas which will form stars ending in the cluster at present time, while bright red points indicate stars which have been already formed by $z = 4.2$. As can clearly be seen, the galaxies that have already been formed are all close to the protocluster region, with only some additional stars already formed along the filaments connecting to the cluster. Thus, large numbers of member galaxies within the protocluster but also its surroundings are good tracers of the currently collapsing large scale structure, and the more such galaxies have already been formed the larger the field of influence for such a cluster. However, the very large structure at such early times is still only partially traced by current star-formation and thus eventually not visible for observations yet. Nevertheless, while large richness is a

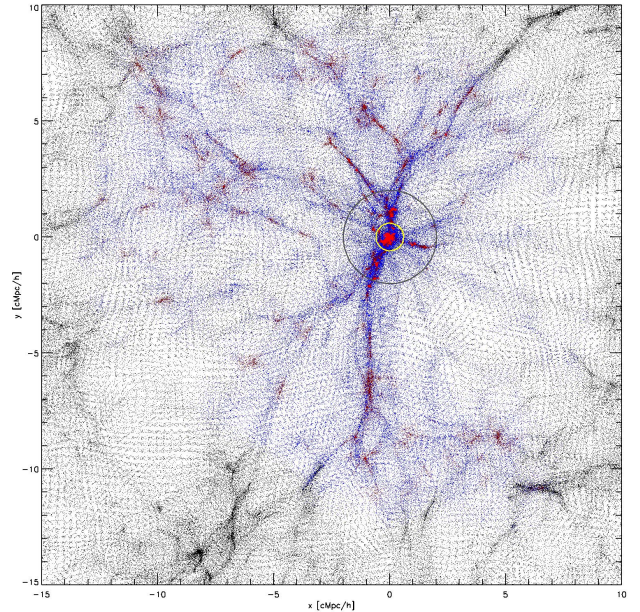


Figure 12. Slice of the Magneticum Box 2b at $z = 4.2$ with a thickness of 5 Mpc/h comoving, centered around protocluster PCl 1. Black dots mark all the gas particles in this slice. Everything that will end up inside the virial radius R_{vir} of the cluster at $z = 0$ that evolved from this protocluster PCl 1 is highlighted in color: Gas particles are marked as blue dots, while those gas particles that end up in the cluster but are transformed into stars by $z = 0$ are shown in dark red. Bright red dots mark the stars that already exist at $z = 4.2$ and all end up in the cluster at $z = 0$. The two circles resemble the virial radii R_{vir} at $z = 4.2$ (small yellow circle) and $z = 0$ (large gray circle). This clearly demonstrates that the protocluster volume at $z = 4.2$ only provides a limited prediction for the future cluster at $z = 0$.

good indicator for a protocluster to evolve into a massive cluster at low redshifts, a small richness is not an indicator that the protocluster cannot evolve into a massive cluster, as also visible from the lower right panel of Fig. 11, as it is very possible that most of the stellar mass is still inside the collapsing filaments and not yet within the virialized area of the protocluster core.

4.2. Forming the BCG and the ICL

As shown in the left panel of Fig. 13, the BCG of our example protocluster PCl 1 (black line) grows very rapidly by 3 orders of magnitude between $z = 7$ and $z = 4$, while at redshift below $z \approx 1 - 2$ the BCG grows much slower than the halo (gray line). The stellar components of all galaxies present within the virial radius of the protocluster at $z = 4.2$ are already nearly completely merged into the BCG (solid red line) at the next available snapshot at $z = 3.4$, and only a very minor stellar component (dashed red line) stays either as satellites or as stripped material within the system towards lower redshift. This is true for all our 8 protocluster candidates, as shown in the right panel of Fig. 13, and in good agreement with

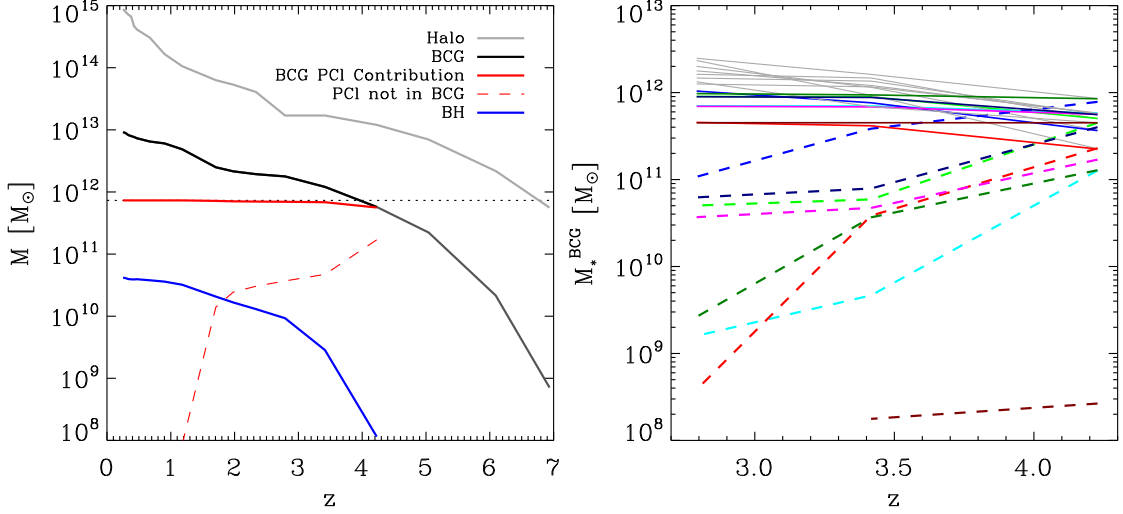


Figure 13. *Left panel:* Mass growth with redshift for the example protocluster PCI 1, for the total (dark plus baryonic) mass M_{vir} (grey line), the stellar mass of the galaxy that is the BCG at $z = 0$ (black line), and the central black hole of that galaxy (blue line). The solid red line shows the contribution of the protocluster stars to the BCG, with the dashed line showing the protocluster stars that are not yet inside the BCG. The dotted black line highlights the total stellar mass that is present already inside the protocluster PCI 1 at $z = 4.2$. *Right panel:* Initial growth phase of the BCGs of the 8 selected example protoclusters. Gray lines show the stellar mass of the galaxy that is the BCG at $z = 0$ (similar to the black line in the left panel), while the colored solid lines show the stellar mass already present in the protoclusters at $z = 4.2$ which has been already accreted onto the BCG at the given redshift. The dashed lines show the stellar mass already present at $z = 4.2$ that is not part of the BCG at the given redshifts.

the results found by Rennehan et al. (2020). This clearly indicates a very short timescale on which these galaxies within the protocluster will merge at this redshift. This timescale is significantly less than 0.42 Gyr, which is the timespan between the stored snapshots, thus it is not possible to obtain more information on the merging processes from the simulation but the simple fact that the merging takes place. Tracing the stellar component further in time reveals that, as expected, these stars that were already part of the protoclusters at $z = 4.2$ mostly end up as part of the present-day BCG, therefore effectively building up the cores of the present-day BCGs.

4.3. Effect of cosmology and simulation volume

Finally, we evaluate the expected mass of the most massive structures at different redshifts, depending on the underlying cosmology. Therefore, we use a new extension of the *Magneticum* simulation set as presented by Singh et al. (2019). These are re-simulations of *Box 1a*, which has a volume of $(896h^{-1}\text{Mpc})^3$, with 2×1526^3 particles, using 15 different cosmologies by varying σ_8 , Ω_0 , H_0 as well as Ω_b . The cosmological parameters for the different runs are listed in Tab. 3. All simulations are run on the lowest available resolution (mr), with a particle resolution of $m_{\text{DM}} = 1.3 \times 10^{10} M_\odot/h$ and $m_{\text{Gas}} = 2.9 \times 10^9 M_\odot/h$ for dark matter and gas, respectively. For details see Singh et al. (2019).

Although these simulations follow the same hydrodynamical treatment and sub-grid physics descrip-

Table 3. Cosmological parameters of the 15 different cosmological runs of *Box1 mr*, as presented by Singh et al. (2019). The gray shaded row corresponds to the setting used for the main suit of the *Magneticum* simulations, especially *Box 2b hr* which is used for the major part of this study.

	Ω_0	Ω_b	σ_8	H_0	f_b
C1	0.153	0.0408	0.614	66.6	0.267
C2	0.189	0.0455	0.697	70.3	0.241
C3	0.200	0.0415	0.850	73.0	0.208
C4	0.204	0.0437	0.739	68.9	0.214
C5	0.222	0.0421	0.793	67.6	0.190
C6	0.232	0.413	0.687	67.0	0.178
C7	0.268	0.0449	0.721	69.9	0.168
C8	0.272	0.0456	0.809	70.4	0.168
C9	0.301	0.0460	0.824	70.7	0.153
C10	0.304	0.0504	0.886	74.0	0.166
C11	0.342	0.0462	0.834	70.8	0.135
C12	0.363	0.0490	0.884	72.9	0.135
C13	0.400	0.0485	0.650	67.5	0.121
C14	0.406	0.0466	0.867	71.2	0.115
C15	0.428	0.0492	0.830	73.2	0.115

tion as the simulation used for the previous part of this study, they have significantly less resolution and therefore we cannot perform a detailed analysis of protoclusters as done before with the much higher resolution simulation of *Box 2b*. Nevertheless, the resolu-

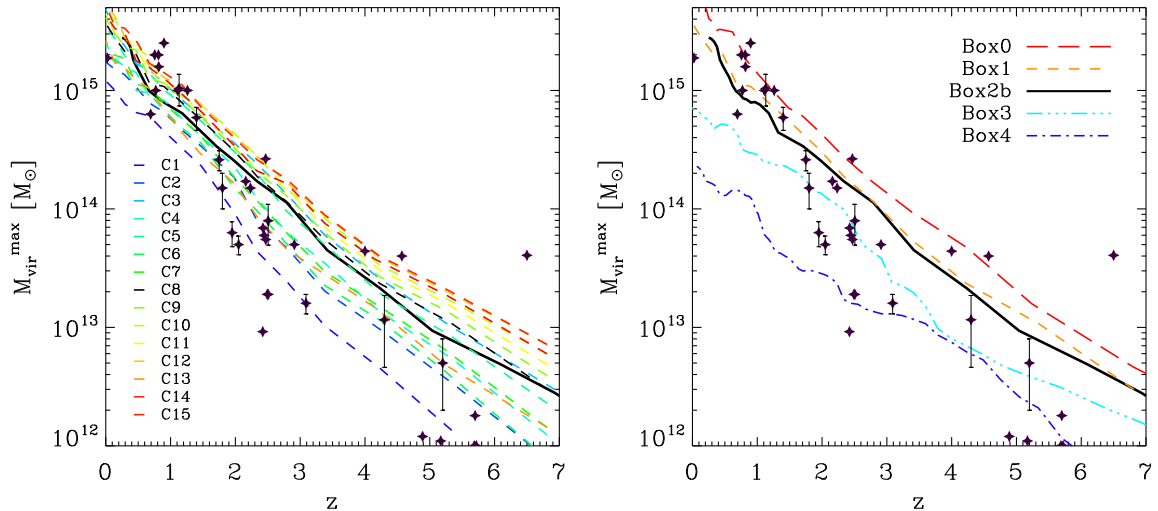


Figure 14. *Left panel:* Similar to Fig. 10, but comparing the observations to the virial mass of the most massive systems from the 15 simulations with different cosmologies (see Tab. 3) at each redshift. Color coding according to the value of σ_8 . For the detailed parameters of the models, see Singh et al. (2019). Star symbols mark all individual (proto)cluster observations from Fig. 10, with the addition of the $z = 6.5$ protocluster from Chanchaiworawit et al. (2019) and the protocluster at $z = 5.2$ from Calvi et al. (2021). Furthermore, a compilation of lower-mass protoclusters at $z > 4.8$ courtesy of F. Sinigaglia is added, sampled from observations by Shimasaku et al. (2003); Venemans et al. (2004); Ouchi et al. (2005); Toshikawa et al. (2012, 2014); Higuchi et al. (2019); Toshikawa et al. (2020). *Right panel:* Same as left panel but for the five different box volumes of the Magneticum Pathfinder simulation suite with the same cosmology. *Box 0* (2688 Mpc/h)³ and *Box 1* (896 Mpc/h)³ are performed with the lowest resolution, *Box 2b* (640 Mpc/h)³ and *Box 3* (128 Mpc/h)³ are performed on high resolution, while *Box 4* (48 Mpc/h)³ is on the highest available resolution.

tion is high enough to predict the expectation of the most massive virial mass as function redshift, similar to the upper limit of the gray shaded area in Fig 10. The colors are the same as used by Singh et al. (2019), and were originally chosen to go from low Ω_m (blue) to a high value of Ω_m (red). Due to choosing the cosmological parameters to follow the current observational constraints within the different figures of merit (for details see Singh et al. (2019)), this means that the different values have non trivial relationships and therefore it is impossible to construct a strict hierarchy of the models. As can be seen from left panel of Fig. 14, the absolute mass of the most massive clusters at high redshift depends mostly on the value of σ_8 , i.e., the larger σ_8 the more massive structures appear already at high redshift, as can be seen especially from the runs C 3 (turquoise line) and C 13 (orange line). Effectively, this results in a different slope for the highest-mass per redshift relation, with flatter slopes for larger values of σ_8 . There is only a small trend with Ω_m , that is larger Ω_m producing larger structures at a given redshift, but this trend is only of secondary order. This clearly shows that measuring the most massive structures present at different redshift can set constraints on the values of σ_8 , and thus protoclusters might be useable as cosmological probes.

Furthermore, we can also see the effect of the different volumes of the simulated boxes from the left panel of Fig. 14, where the solid black line marks the most massive halos per redshift for the smaller but

higher resolved simulation *Box 2b*, in comparison to the black dashed line that marks the *Box 1a* cosmological run (C 8) with the same cosmology as the *Box 2b* simulation used for most of this work. The low resolution simulation of *Box 1a* (dashed line) has roughly 3 times the volume of the high resolution simulation *Box 2b* (solid line), showing a mild trend to harbour larger structures, as expected due to the larger cosmological modes included in the larger simulation volumes, independent of the resolution. This is also further highlighted in the right panel of Fig. 14, where the most massive structures per redshift are shown for all five volumes that are part of the Magneticum pathfinder simulation suite (with the same cosmology as *Box 2b*). This clearly demonstrates the need for large enough box volume simulations to capture those massive protoclusters that are now detected at high redshifts and study their properties and evolution pathways.

4.4. Predictions to $z = 10$

Finally, we extend our study of the most massive already bound systems with redshift towards even higher redshifts of $z = 10$, the highest redshift at which already bound halos with stellar components can be found in the simulations given the resolution limits. We predict that halo masses of up to $M_{\text{vir}} = 1 \times 10^{12} M_{\odot}$ can already be found at $z = 9$, as shown in Fig. 15, and a few times $10^{11} M_{\odot}$ at $z = 10$. As can also be seen, the massive protocluster at $z = 6.5$ presented by Chanchaiworawit et al. (2019)

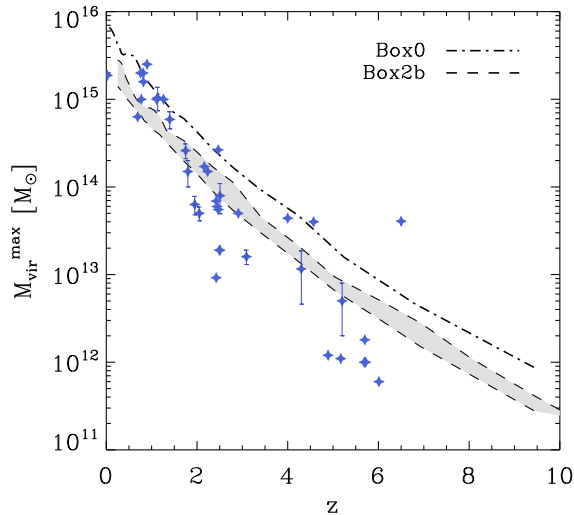


Figure 15. Similar to Fig 10, but extended as predictions of the highest expected total masses to be found up to redshifts of $z = 10$, using the two largest box volumes from the Magneticum pathfinder suite of simulations at low *Box 0* ($2688 \text{ Mpc}/h^3$) and high *Box 2b* ($640 \text{ Mpc}/h^3$) resolutions. For *Box 2b*, at each redshift the mass range of the 10 most massive systems is shown as gray shaded area, while for *Box 0* only the line for the most massive system per redshift is shown. A compilation of observed systems as described in Fig 10 with the addition of the high redshift $z = 6.5$ protocluster from Chanchaiworawit et al. (2019) and the protocluster at $z = 5.2$ from Calvi et al. (2021) is shown as blue stars. Furthermore, a compilation of lower-mass protoclusters at $z > 4.8$ courtesy of F. Sinigaglia is added, sampled from observations by Shimasaku et al. (2003); Venemans et al. (2004); Ouchi et al. (2005); Toshikawa et al. (2012, 2014); Higuchi et al. (2019); Toshikawa et al. (2020).

has a mass larger than any of our simulations, even the largest simulation volume, can reproduce, albeit the error bars are rather large. Whether this indicates that none of our simulation volumes is large enough to capture such massive structures, if that particular object is an outlier, or if the mass could be overestimated is beyond the scope of this work, but will be interesting to investigate in the future. All other systems reported at redshifts above $z = 4.2$ are well within the predicted mass range from our simulation.

5. DISCUSSION AND CONCLUSION

Utilizing the very large cosmological hydrodynamical simulation *Box 2b* of the *Magneticum* project, which includes a sub-resolution treatment of star formation, stellar evolution and a treatment of the effect of super massive black holes, we show that such simulations, once the volume is large enough, can successfully produce massive protoclusters like *SPT2349-56*, reproducing many of their physical properties. Especially, we find several virialized structures at $z = 4.2$ with a similar number of member galaxies (richness) and the same dynamical properties of the member galaxies

as the observed protocluster *SPT2349-56* at $z = 4.3$ (Miller et al. 2018; Rotermund et al. 2021), but also similar to the protocluster core found by Oteo et al. (2018) at $z = 4$. The simulations also predict that several of the member galaxies of these structures are fast rotating systems, in agreement with the observed findings for member galaxies of *SPT2349-56*.

We find that these member galaxies of the protoclusters at $z = 4.2$ will merge on very short timescales, forming the progenitors of today’s cluster BCGs, in agreement with results found by Rennehan et al. (2020). The stellar component merging from these satellite galaxies assembles to build up the core of the BCG, and indicating that the centres of today’s massive BCGs echo this fast growing phase and their central velocity dispersion may reflect the dynamics of the galaxies within these protoclusters, being significant smaller than the velocity dispersion of the present-day clusters the BCG lives in (see Sohn et al. 2019; Bender et al. 2015; Remus et al. 2017).

However, while the general stellar and total masses of the simulated protoclusters and the number and dynamics of member galaxies within resemble the observations closely, the instantaneous integrated star-formation rate within such simulated protoclusters is a factor $\approx 2 \dots 3$ smaller than the observed values, although the simulations are reproducing the observed integrated gas mass within the protoclusters. As the simulations also reasonably well reproduce the main sequence of star-forming galaxies as well as the observed stellar mass function up to this redshift, this indicates that the star-formation in the simulations lacks the ability to reproduce higher star-formation efficiency (or accordingly lower depletion timescales) at least in certain environments. The reason for this issue can be found most likely in the implementation of the star formation process that currently assumes a rather continuous star formation and a Schmitt-Kennicutt relation that holds true even at high redshifts, an issue that needs to be addressed in future simulations.

While star forming galaxies are detectable in the high redshift protoclusters due to their large gas reservoirs, the quiescent galaxies at high redshifts are much more elusive. Using our sample of 42 simulated protoclusters, we find that there can already be quenched galaxies in such protoclusters, albeit their number is low, and on average at the total mass range of such protoclusters (around $10^{13} M_\odot$) barely at 10%. Their quiescent fractions do not depend on the dynamical state of the protocluster, neither its virial mass nor the overall star formation rate or the richness. We compare our quiescent fractions to observations at lower redshifts where quiescent fractions can actually be inferred (Strazzullo et al. 2019; Sarron & Conselice 2021), and find an overall agreement, in agreement with previous work done by Lotz et al. (2019, 2021). We find the quiescent fraction to overall strongly in-

crease with decreasing redshift, even at fixed total mass, clearly showing that quenching becomes more efficient at lower redshifts in both group and cluster environments.

The simulations predict that the star-forming gas in protoclusters at redshifts of $z \approx 4$ is already enriched to roughly solar values. Part of this cold gas is expected to be subsequently heated by feedback and become part of the intra-cluster medium of the forming galaxy cluster. About half of the gas within these structures at $z = 4.2$ is already significantly heated to temperatures around 1keV, and a very small fraction ($\approx 2\%$) of this hot gas is already enriched to one tenth of the solar value.

Using the full power of the simulation, we traced the protoclusters identified at $z = 4.2$ down to $z = 0$, to test the hypothesis that the extremely massive structures found at high redshifts really are the progenitors of the most massive galaxy clusters at present day. However, at $z \approx 4$, these protocluster regions reflect only a very minor part of the Lagrangian region which will collapse into the final galaxy clusters at $z = 0$, and therefore none of the protocluster properties at $z = 4.2$ (e.g., virial mass, star-formation rate, stellar mass, or richness in members) proves to be a good proxy for the mass of the final cluster at $z = 0$. In fact, from our 8 examples chosen to be among the top in these measures at $z = 4.2$, none is among the 10 most massive clusters at $z = 0$. Even more striking, one of them evolves barely into a very low mass cluster with a virial mass of less than $1 \times 10^{14} M_{\odot}$. From the full sample of 42 protoclusters at $z = 4.2$, four do not even grow above the mass of $1 \times 10^{14} M_{\odot}$. This is due to the fact that nodes in the cosmic web can collapse at very different timescales, and some of the nodes that collapse rather early starve and become fossil systems. With respect to the observable quantities within protoclusters at high redshift, we find the richness in galaxy members to be the only quantity that has a slight indication for the future of the system, in that rich systems tend to also evolve into massive systems at $z = 0$, however, the opposite is not true as also some systems that are low in richness at $z = 4.2$ evolve into massive clusters at present-day.

Utilizing a second set of simulations from the *Magneticum* pathfinder suite of simulations, which were performed with 15 different cosmologies (Singh et al. 2019), we quantified the expected largest mass of bound systems with redshift. Given the current uncertainties in the actual values of the cosmological parameters, we showed that the highest mass per redshift is actually a good tracer for σ_8 , with the discrepancies larger the higher the redshift. Thus, finding the most massive bound systems at high redshifts can set constraints on those cosmological parameters.

To conclude, we found that, on one hand, various aspects of observed protoclusters can be successfully reproduced by current state-of-the-art cos-

mological simulations if the simulation volumes are large enough. These protocluster structures have already virialized cores, already hosting a significant hot atmosphere which could be targeted observationally. On the other hand, detailed comparisons of the star-formation rates reveal, as indicated in previous work from various simulation suites, that there seems to be some environmental increase in star-formation efficiency (or accordingly reduced depletion timescales) which current sub-resolution models describing the star-formation within the simulations are not able to capture, albeit gas masses and both the general star formation main sequence and the stellar mass functions are reproduced successfully. While some of the protocluster systems found at $z \approx 4$ evolve into massive clusters at $z = 0$, they are not among the progenitors of today's most massive clusters, and some of them barely reach cluster masses. Overall, the simulations shape a picture of a fast growing mode of massive systems at early time, which should still be echoed in the dynamical properties of the central parts of today's massive BCGs, with a broad range of outcome in total mass at low redshifts.

ACKNOWLEDGEMENTS

We especially thank Scott Chapman for several helpful discussion, Florian Sarron for providing the data from the Detectivz survey in mass bins comparable to the simulated cuts, and Olivier Gilbert for providing the COSMOS data in redshift bins comparable to the simulation outputs. Furthermore, we would like to thank Francesco Sinigaglia for compiling and providing a high redshift protocluster sample, and Giulia Rodighiero for helpful comments. The *Magneticum* simulations were performed at the Leibniz-Rechenzentrum with CPU time assigned to the Project *pr83li*. This work was supported by the Deutsche Forschungsgemeinschaft (DFG, German Research Foundation) under Germany's Excellence Strategy – EXC-2094 – 390783311. KD acknowledges support by the COMPLEX project from the European Research Council (ERC) under the European Union's Horizon 2020 research and innovation program grant agreement ERC-2019-AdG 882679. HD acknowledges financial support from the Agencia Estatal de Investigación del Ministerio de Ciencia e Innovación (AEI-MCINN) under grant *La evolución de los cúmulos de galaxias desde el amanecer hasta el mediodía cósmico* with reference PID2019-105776GB-I00/DOI:10.13039/501100011033, and support from the ACIISI, Consejería de Economía, Conocimiento y Empleo del Gobierno de Canarias and the European Regional Development Fund (ERDF) under grant with reference PROID2020010107. We are especially grateful for the support by M. Petkova through the Computational Center for Particle and Astrophysics (C2PAP).

REFERENCES

- Ando, M., Shimasaku, K., Momose, R., et al. 2022, arXiv e-prints, arXiv:2201.05185
- Aoyama, K., Kodama, T., Suzuki, T. L., et al. 2022, *ApJ*, 924, 74
- Bassini, L., Rasia, E., Borgani, S., et al. 2020, *A&A*, 642, A37
- Beck, A. M., Murante, G., Arth, A., et al. 2016, *MNRAS*, 455, 2110
- Bender, R., Kormendy, J., Cornell, M. E., & Fisher, D. B. 2015, *ApJ*, 807, 56
- Biffi, V., Planelles, S., Borgani, S., et al. 2017, *MNRAS*, 468, 531
- Biffi, V., Planelles, S., Borgani, S., et al. 2018, *MNRAS*, 476, 2689
- Bocquet, S., Saro, A., Dolag, K., & Mohr, J. J. 2016, *MNRAS*, 456, 2361
- Calvi, R., Dannerbauer, H., Arrabal Haro, P., et al. 2021, *MNRAS*, 502, 4558
- Calvi, R., Rodríguez Espinosa, J. M., Mas-Hesse, J. M., et al. 2019, *MNRAS*, 489, 3294
- Chanchaiworawit, K., Guzmán, R., Salvador-Solé, E., et al. 2019, *ApJ*, 877, 51
- Chiang, Y.-K., Overzier, R., & Gebhardt, K. 2013, *ApJ*, 779, 127
- Cooke, K. C., Kartaltepe, J. S., Tyler, K. D., et al. 2019, *ApJ*, 881, 150
- Cucciati, O., Lemaux, B. C., Zamorani, G., et al. 2018, *A&A*, 619, A49
- Daddi, E., Valentino, F., Rich, R. M., et al. 2021, *A&A*, 649, A78
- Dannerbauer, H., Kurk, J. D., De Breuck, C., et al. 2014, *A&A*, 570, A55
- Dannerbauer, H., Lehnert, M. D., Emonts, B., et al. 2017, *A&A*, 608, A48
- Davidzon, I., Ilbert, O., Laigle, C., et al. 2017, *A&A*, 605, A70
- Dolag, K., Borgani, S., Murante, G., & Springel, V. 2009, *MNRAS*, 399, 497
- Dolag, K., Jubelgas, M., Springel, V., Borgani, S., & Rasia, E. 2004, *ApJL*, 606, L97
- Dolag, K., Mevius, E., & Remus, R.-S. 2017, *Galaxies*, 5, 35
- Dolag, K., Vazza, F., Brunetti, G., & Tormen, G. 2005, *MNRAS*, 364, 753
- Donnert, J., Dolag, K., Brunetti, G., & Cassano, R. 2013, *MNRAS*, 429, 3564
- Fabjan, D., Borgani, S., Tornatore, L., et al. 2010, *MNRAS*, 401, 1670
- Franx, M., van Dokkum, P. G., Förster Schreiber, N. M., et al. 2008, *ApJ*, 688, 770
- Genzel, R., Tacconi, L. J., Gracia-Carpio, J., et al. 2010, *MNRAS*, 407, 2091
- Gómez-Guijarro, C., Riechers, D. A., Pavesi, R., et al. 2019, *ApJ*, 872, 117
- Granato, G. L., Ragone-Figueroa, C., Domínguez-Tenreiro, R., et al. 2015, *MNRAS*, 450, 1320
- Harikane, Y., Ouchi, M., Ono, Y., et al. 2019, *ApJ*, 883, 142
- Harris, W. E., Remus, R.-S., Harris, G. L. H., & Babyk, I. V. 2020, *ApJ*, 905, 28
- Hatch, N. A., Cooke, E. A., Muldrew, S. I., et al. 2017, *MNRAS*, 464, 876
- Higuchi, R., Ouchi, M., Ono, Y., et al. 2019, *ApJ*, 879, 28
- Hirschmann, M., Dolag, K., Saro, A., et al. 2014, *MNRAS*, 442, 2304
- Ilbert, O., McCracken, H. J., Le Fèvre, O., et al. 2013, *A&A*, 556, A55
- Jones, G. C., Vergani, D., Romano, M., et al. 2021, arXiv e-prints, arXiv:2104.03099
- Kim, J., Jee, M. J., Perlmutter, S., et al. 2019, arXiv e-prints, arXiv:1910.04775
- Kodama, T., Tanaka, I., Kajisawa, M., et al. 2007, *MNRAS*, 377, 1717
- Komatsu, E., Smith, K. M., Dunkley, J., et al. 2011, *ApJS*, 192, 18
- Kubo, M., Uchimoto, Y. K., Yamada, T., et al. 2013, *ApJ*, 778, 170
- Kubo, M., Umehata, H., Matsuda, Y., et al. 2021, *ApJ*, 919, 6
- Kubo, M., Yamada, T., Ichikawa, T., et al. 2016, *MNRAS*, 455, 3333
- Kubo, M., Yamada, T., Ichikawa, T., et al. 2017, *MNRAS*, 469, 2235
- Leung, T. K. D., Riechers, D. A., Baker, A. J., et al. 2019, *ApJ*, 871, 85
- Lim, S., Scott, D., Babul, A., et al. 2021, *MNRAS*, 501, 1803
- Lotz, M., Dolag, K., Remus, R.-S., & Burkert, A. 2021, *MNRAS*, 506, 4516
- Lotz, M., Remus, R.-S., Dolag, K., Biviano, A., & Burkert, A. 2019, *MNRAS*, 488, 5370
- Ludlow, A. D., Fall, S. M., Schaye, J., & Obreschkow, D. 2021, *MNRAS*, 508, 5114
- Ludlow, A. D., Schaye, J., Schaller, M., & Bower, R. 2020, *MNRAS*, 493, 2926
- Lustig, P., Strazzullo, V., Remus, R.-S., et al. 2022, arXiv e-prints, arXiv:2201.09068
- McConachie, I., Wilson, G., Forrest, B., et al. 2022, *ApJ*, 926, 37
- Miller, T. B., Chapman, S. C., Aravena, M., et al. 2018, *Nature*, 556, 469
- Muldrew, S. I., Hatch, N. A., & Cooke, E. A. 2015, *MNRAS*, 452, 2528
- Oteo, I., Ivison, R. J., Dunne, L., et al. 2018, *ApJ*, 856, 72
- Ouchi, M., Shimasaku, K., Akiyama, M., et al. 2005, *ApJL*, 620, L1
- Overzier, R. A. 2016, *A&A Rv*, 24, 14

- Pavesi, R., Riechers, D. A., Sharon, C. E., et al. 2018, *ApJ*, 861, 43
- Pearson, W. J., Wang, L., Hurley, P. D., et al. 2018, *A&A*, 615, A146
- Ragagnin, A., Dolag, K., Biffi, V., et al. 2017, *Astronomy and Computing*, 20, 52
- Ragagnin, A., Dolag, K., Moscardini, L., Biviano, A., & D’Onofrio, M. 2019, *MNRAS*, 486, 4001
- Ragone-Figueroa, C., Granato, G. L., Ferraro, M. E., et al. 2018, *MNRAS*, 479, 1125
- Remus, R.-S., Dolag, K., & Hoffmann, T. 2017, *Galaxies*, 5, 49
- Rennehan, D., Babul, A., Hayward, C. C., et al. 2020, *MNRAS*, 493, 4607
- Rotermund, K. M., Chapman, S. C., Phadke, K. A., et al. 2021, *MNRAS*, 502, 1797
- Santini, P., Fontana, A., Castellano, M., et al. 2017, *ApJ*, 847, 76
- Saro, A., Borgani, S., Tornatore, L., et al. 2009, *MNRAS*, 392, 795
- Sarron, F. & Conselice, C. J. 2021, *MNRAS*, 506, 2136
- Shi, K., Lee, K.-S., Dey, A., et al. 2019, *ApJ*, 871, 83
- Shimakawa, R., Kodama, T., Tadaki, K. I., et al. 2014, *MNRAS*, 441, L1
- Shimakawa, R., Koyama, Y., Röttgering, H. J. A., et al. 2018, *MNRAS*, 481, 5630
- Shimasaku, K., Ouchi, M., Okamura, S., et al. 2003, *ApJL*, 586, L111
- Singh, P., Saro, A., Costanzi, M., & Dolag, K. 2019, *arXiv e-prints*, arXiv:1911.05751
- Smit, R., Bouwens, R. J., Carniani, S., et al. 2018, *Nature*, 553, 178
- Sohn, J., Geller, M. J., Diaferio, A., & Rines, K. J. 2019, *arXiv e-prints*, arXiv:1910.11192
- Springel, V., White, S. D. M., Tormen, G., & Kauffmann, G. 2001, *MNRAS*, 328, 726
- Steinborn, L. K., Dolag, K., Hirschmann, M., Prieto, M. A., & Remus, R.-S. 2015, *MNRAS*, 448, 1504
- Strazzullo, V., Coogan, R. T., Daddi, E., et al. 2018, *ApJ*, 862, 64
- Strazzullo, V., Daddi, E., Gobat, R., et al. 2015, *A&A*, 576, L6
- Strazzullo, V., Daddi, E., Gobat, R., et al. 2016, *ApJL*, 833, L20
- Strazzullo, V., Gobat, R., Daddi, E., et al. 2013, *ApJ*, 772, 118
- Strazzullo, V., Pannella, M., Mohr, J. J., et al. 2019, *A&A*, 622, A117
- Teklu, A. F., Remus, R.-S., Dolag, K., et al. 2015, *ApJ*, 812, 29
- Teklu, A. F., Remus, R.-S., Dolag, K., & Burkert, A. 2017, *MNRAS*, 472, 4769
- Tomczak, A. R., Lemaux, B. C., Lubin, L. M., et al. 2017, *MNRAS*, 472, 3512
- Tornatore, L., Borgani, S., Dolag, K., & Matteucci, F. 2007, *MNRAS*, 382, 1050
- Tornatore, L., Borgani, S., Matteucci, F., Recchi, S., & Tozzi, P. 2004, *MNRAS*, 349, L19
- Toshikawa, J., Kashikawa, N., Ota, K., et al. 2012, *ApJ*, 750, 137
- Toshikawa, J., Kashikawa, N., Overzier, R., et al. 2014, *ApJ*, 792, 15
- Toshikawa, J., Malkan, M. A., Kashikawa, N., et al. 2020, *ApJ*, 888, 89
- Übler, H., Genzel, R., Wisnioski, E., et al. 2019, *ApJ*, 880, 48
- Umehata, H., Tamura, Y., Kohno, K., et al. 2015, *ApJL*, 815, L8
- van de Sande, J., Lagos, C. D. P., Welker, C., et al. 2019, *MNRAS*, 484, 869
- Venemans, B. P., Röttgering, H. J. A., Overzier, R. A., et al. 2004, *A&A*, 424, L17
- Wang, T., Elbaz, D., Daddi, E., et al. 2016, *ApJ*, 828, 56
- Wang, T., Elbaz, D., Daddi, E., et al. 2018, *ArXiv e-prints* [1810.10558]
- Wiersma, R. P. C., Schaye, J., & Smith, B. D. 2009, *MNRAS*, 393, 99
- Yonekura, N., Kajisawa, M., Hamaguchi, E., Mawatari, K., & Yamada, T. 2021, *arXiv e-prints*, arXiv:2109.02019
- Zhang, Y., Zheng, X., Shi, D., et al. 2022, *arXiv e-prints*, arXiv:2203.09260